Sindre Mjøen Svendsen

Defects and ferroelectricity in LaWN$_3$

Master's thesis in Material Science and Engineering
Supervisor: Sverre M. Selbach
Co-supervisor: Benjamin A. D. Williamson and Kristoffer Eggestad
June 2024

Master's thesis

◘ **NTNU**

Norwegian University of
Science and Technology

Sindre Mjøen Svendsen

Defects and ferroelectricity in LaWN₃

Master's thesis in Material Science and Engineering
Supervisor: Sverre M. Selbach
Co-supervisor: Benjamin A. D. Williamson and Kristoffer Eggestad
June 2024

Norwegian University of Science and Technology
Faculty of Natural Sciences
Department of Materials Science and Engineering

NTNU
Norwegian University of
Science and Technology

Preface

This master thesis was conducted in the spring of 2024 and is the result of the course *TMT4905 - Materials Technology, Master's Thesis* at the Department of Materials Science and Engineering at the Norwegian University of Science and Technology, NTNU. This study is a continuation of my project thesis on the bulk properties of the perovskite nitride $LaWN_3$, "Holes in the $LaWN_3$" [1].

Acknowledgements

I would like to thank my supervisors Professor Sverre M. Selbach, Post doc. Dr. Benjamin A. D. Williamson and PhD candidate Kristoffer Eggestad for the helpful discussions and guidance for the simulations, as the project would not be possible without their help. Secondly, I would like to thank the FACET ferroics group for the feedback during the project, as well as interesting presentations broadening by knowledge in the field of ferroics. Lasty, I would like to thank my family and my classmates I have had the pleasure to study with during my time at NTNU.

Sindre Mjøen Svendsen
Trondheim, Norway
June, 2024

Abstract

In the pursuit of better and more reliable memory devices, significant efforts have been spent on the development of ferroelectric devices as non-volatile random-access memory (NVRAM). Ferroelectric random-access memory (FeRAM) has the advantage over other NVRAM technologies by having a low power consumption and excellent endurance, but FeRAM devices are limited in storage density. To increase the storage density of FeRAM, researchers have tried to use ferroelectric domain walls instead of the domains to store data. However, practical use of FeRAM using domain walls remain challenging due to low conductivity in the domain walls.

LaWN$_3$ is a ferroelectric perovskite nitride that shows potential for having conducting domain walls. From previous work [1], the band gap in the structure has been closely linked to the position of the tungsten atom in the nitrogen octahedra. In the domain wall, the polarization switches direction and the position of the tungsten atom will be closer to the center of the octahedron. This shift in the tungsten position results in a lower band gap and enhanced conductivity of the domain wall compared to bulk. Because the angle of the primitive unit cell in LaWN$_3$ is close to the ideal 60 degree cell angle, the ferroelastic 71° and 109° domain walls will likely be formed together with the 180° domain wall.

The domain walls and defects in LaWN$_3$ have been investigated with first-principle calculations using density functional theory. Structural parameters were followed for the different domain walls and the formation energy was calculated. To study the possibility of conducting domain walls in LaWN$_3$, layer-resolved densities of states were calculated. The formation energy of intrinsic defects and oxygen substitution of nitrogen was calculated for different chemical potentials in the stability window of LaWN$_3$. Transition level diagrams were constructed for various defects and nudged elastic band calculations were performed on nitrogen and lanthanum vacancies in the structure, to get a better understanding of the defect chemistry of nitride perovskites.

The 71° domain wall had the lowest formation energy and is thus likely to dominate. A significant reduction in the band gap from the bulk state was found for all the domain walls, with the 180° domain wall showing a metallic density of states in the domain wall. This indicates a significant increase in the conductivity of the domain wall compared to bulk. Nitrogen vacancies had the lowest formation energy of the considered defects with a transition level to a neutral defect close to the conduction band. Therefore, it is likely that a significant amount of charge carriers is introduced into the structure through defects. The migration barrier for nitrogen vacancies in LaWN$_3$ is surprisingly low, which may result in an accumulation of nitrogen vacancies in the domain wall, and that LaWN$_3$ does not exhibit the predicted better thermal stability than oxygen perovskites.

To conclude, the large reduction in the band gap observed in the domain walls in LaWN$_3$ suggests that LaWN$_3$ could potentially be used in ferroelectric memory devices instead of the current state-of-the-art. The migration barrier found for defects in LaWN$_3$ are similar to what is found in oxide perovskites, suggesting that LaWN$_3$ has similar refractory stability compared to the oxide counterparts.

Sammendrag

I jakten på bedre og mer pålitelige minneenheter, har det blitt lagt stor innsats i utviklingen av ferroelektriske enheter til non-volatile random-access memory (NV-RAM). Fordelen ferroelektrisk random-access memory (FeRAM) har over annen NV-RAM teknologi er at den bruker mindre energi og har god holdbarhet, men FeRAM enheter har begrenset lagringstetthet. For å øke lagringstettheten har forskere prøvd å bruke ferroelektriske domenevegger i stedet for domenene til datalagring. Praktisk bruk av FeRAM som bruker domenevegger har fortsatt utfordringer med lav strøm fra domeneveggene.

$LaWN_3$ er et ferroelektrisk nitrid-perovskitt som viser potensiale for elektrisk ledende domenevegger. Det er tidligere vist at båndgapet i strukturen er avhengig av posisjonen til wolframatomet i nitrogen oktaederet [1]. I domeneveggen bytter polariseringen retning og wolframatomet flytter seg nærmere sentrum av oktaederet. Endringen i posisjonen til wolframatomet vil gi et mindre båndgap og økt ledningsevne i domeneveggene sammenlignet med bulk. Vinkelen i den primitive enhentscellen i $LaWN_3$ ligger nært den ideelle 60 graders vinkelen, noe som medfører at de ferroelastiske 71° og 109° domeneveggene også kan dannes sammen med 180° domeneveggen.

Domeneveggene og defekter i $LaWN_3$ har blitt undersøkt med *ab initio* beregninger ved å benytte density functional theory. Strukturelle parametere ble fulgt for de forskjellige domeneveggene og dannelsesenergien ble beregnet. For å studere muligheten for ledende domenevegger i $LaWN_3$ ble layer-resolved densities of states beregnet. Dannelsesenergien for iboende defekter og oksygensubsititusjon av nitrogenatomet ble beregnet for forskjellige kjemiske potensialene i stabilitetsvinduet for $LaWN_3$. Overgangstilstandsdiagrammer ble laget for de ulike defektene og nudged elastic band beregninger ble utført på nitrogen- og lantan-vakanser i strukturen, for å få bedre forståelse for defektkjemien i nitrid-perovskitter.

Dannelsesenergien var lavest for 71° domeneveggen som sannsynligvis vil dominere. En signifikant reduksjon i båndgapet fra bulk ble funnet for alle domeneveggene, med metallisk density of states for 180° domeneveggen. Dette indikerer en signifikant økning i ledningsevne for domeneveggen sammenlignet med bulk. Av defektene hadde nitrogenvakansene lavest dannelsesenergi med en overgangstilstand til en nøytral defekt nær ledningsbåndet. Det er derfor sannsynlig at en signifikant mengde ladningsbærere vil bli introdusert i strukturen gjennom defekter. Migrasjonsbarrieren for nitrogenvakanser i $LaWN_3$ var overraskende lav, noe som kan betyr at nitrogenvakansene samler seg i domeneveggene, og at $LaWN_3$ ikke har bedre termiske stabiliteten enn oksid-perovskitter som forventet.

For å konkludere, viser alle domeneveggene en stor reduksjon i båndgap, noe som betyr at $LaWN_3$ kan potensielt brukes som ferroelektrisk minne teknologi i stedet for dagens beste teknologi. Migrasjonsbarrieren som ble funnet for defekter i $LaWN_3$ er lik hva som er observert i oksid-perovskitter, noe som indikerer at $LaWN_3$ har lik termisk stabilitet sammenlignet som oksid-perovskitter.

Abbreviations

NVRAM = Non-Volatile Random-Access Memory
FeRAM = Ferrroelectric Random-Access Memory
DFT = Density Functional Theory
VBM = Valence Band Maximum
CBM = Conduction Band Minimum
SE = Schrödinger equation
DoS = Density of States
DW = Domain Wall
NEB = Nudged Elastic Band

Table of Contents

List of Figures

List of Tables

1   Introduction

Alan Turing published the theoretical foundation of the modern general computer in 1936 [2]. The general computer sparked the explosive evolution of the information age, a rapid shift from the economy from the industrial revolution to the economy of information technology. The information age is a direct consequence of the rise in computational power due to the rapid evolution of the miniaturization of modern computer with better and smaller components. This advancement in technology is described by Moore´s law, stating that the number of transistors in an integrated circuit is doubled every second year. Since 1971, the transistor density in logic circuits has increased more than 600 000-fold [3]. Components need to be ever smaller and more efficient to match the requirements of the technological evolution. However, the growth in computational power is accompanied with a large increase in power consumption. Computers contribute to 34% of the total IT energy consumption yearly [4]. This is more than 3 times the yearly energy consumption of Norway [5][6]. A small improvement in device performance can therefore have a large impact on the total power consumption of computers.

As computers grow more powerful, the need for better and more reliable computer memory devices is continuously increased. In this pursuit, considerable efforts have been made to replace the current RAM memory to non-volatile random-access memory (NVRAM). NVRAM is used to store data without power being applied. If all memory of the computer was of the NVRAM type, the startup time for a computer after a power interruption would be reduced greatly. However, current NVRAM technologies have limitations with power consumption when writing data, storage density and endurance [7]. These are properties needed to replace the current RAM technology, not only for the performance, but also the sustainability of the device.

Ferroelectric materials are a class of material which have been proposed for new logical and memory devices, like ferroelectric random-access memory (FeRAM) and ferroelectric field effect transistors. A ferroelectric material has a polarization which is switchable by an external electric field. Since the polarization is switchable, it can be used to store binary numbers. The different polarization directions represent the stored zeros and ones. The storage density of the devices is thus limited to the size of the ferroelectric domains, which is the area with a coherent specific polarization direction. The FeRAM devices commercially available today are made with the perovskite PZT and works as an NVRAM [8]. The advantage with FeRAM is low power usage, excellent endurance and good writing speed, but is limited in storage density compared to modern transistors.

The interface between two domains with different polarization direction in a ferroelectric material is called a ferroelectric domain wall. The domain wall has gathered interest due to the different properties of the domain wall compared to the bulk phase and the fact that the domain walls are a homo-interface. The domain walls are much smaller than the domains themselves, which results in a higher storage density if FeRAMs could use the domain walls as the storage unit instead of the domains. Domain walls are homo-interfaces, they can be moved in the structure

and therefore it is possible to write and erase data with the domain walls. Sharma et. al [9] were in 2017 able to make a prototype of a memory device, using ferroelectric domain walls. The device was based on the increased conductivity in the domain wall in the perovskite oxide $BiFeO_3$, compared to bulk conductivity in the domains. They were able to make the device with a component size of 100 nm, which is smaller than the current commercial FeRAMs. However, the domain wall current was not large enough for a useful device application, but the research confirmed the famous quote from Nobel laureate Herbert Kroemer, "the interface is the device" [10][11]. To develop this concept further towards practical applications it is important to explore perovskites containing domain walls with larger conductivity, to create a practical usable FeRAM based on conducting domain walls.

$LaWN_3$ is a ferroelectric perovskite nitride which have gained the interest of researchers in the last decade. Perovskite nitrides are not well studied, and only a few have been synthesised, $LaWN_3$ being one of them. What spurs the interest is that $LaWN_3$ exhibit a large polarization, and a desirable band gap for optoelectronic applications. From my previous study [1], it was found that the band gap in $LaWN_3$ is closely related to the displacement of the tungsten atom, indicating conducting domain walls in the material. However, many properties of $LaWN_3$ are still unknown, but there is no doubt that $LaWN_3$ represent one of the most exciting unexplored perovskites.

1.1 Aim

The aim of this study is to investigate the domain structure and properties of $LaWN_3$ in addition to the largely unknown defect chemistry. This will be done through Density Functional Theory (DFT) simulations and is a continuation of previous work done by the author [1]. The electronic and structural properties of the domain walls in $LaWN_3$ will be investigated for the potential for conducting domain walls for the use in ferroelectric memory devices. The defect chemistry of $LaWN_3$ will be investigated to improve synthesis processes and conditions, as well as to get a better understanding of defect chemistry in nitride perovskite, compared to the well-studied oxide and halide perovskite counterparts.

2 Previous work

This project is a continuation of the project thesis "Holes in the $LaWN_3$" [1]. In this study, the structural and electronic bulk properties of $LaWN_3$ were investigated using density functional theory (DFT). The $R3c$ structure was identified as the lowest energy configuration and found to be dynamically stable through phonon dispersion calculations. The $Pmc2_1$ space group was the closest lying structure in energy and was also dynamically stable. $LaWN_3$ was found to have bulk and shear modulus larger than typical perovskite oxides, combined with a large spontaneous polarization. These are properties that enables the use of $LaWN_3$ in high pressure and temperature applications. The dielectric tensor was also calculated, showing higher response to electric fields than common oxide perovskites like $BaTiO_3$, $LiNbO_3$ and $BiFeO_3$.

The path $R3c \rightarrow R\overline{3}c \rightarrow Pm\overline{3}m$ was suggested as a transition path to a high temperature phase. This suggestion was based on the formation energy of the different space groups and allowed second order transitions from group theory.

The DoS and electronic band structure were calculated for different rhombohedral space groups of $LaWN_3$. The band gap found for ground state $R3c$ structure was 0.94 eV using PBEsol and 2.06 eV using a hybrid functional. The band gap was found to be strongly dependent on the displacement of tungsten in the nitrogen octahedra, explained by the second order Jahn-Teller effect. The displacement of the central atom in a polar structure gives a non-zero overlap of atomic orbitals, lowering the energy of the bonding orbitals and increasing the energy of the antibonding orbitals, thus increasing the band gap, see Figure 2.1. The effect was strong enough to close the band gap for the non-polar structures, even with a hybrid functional, suggesting $LaWN_3$ could have conducting domain walls.
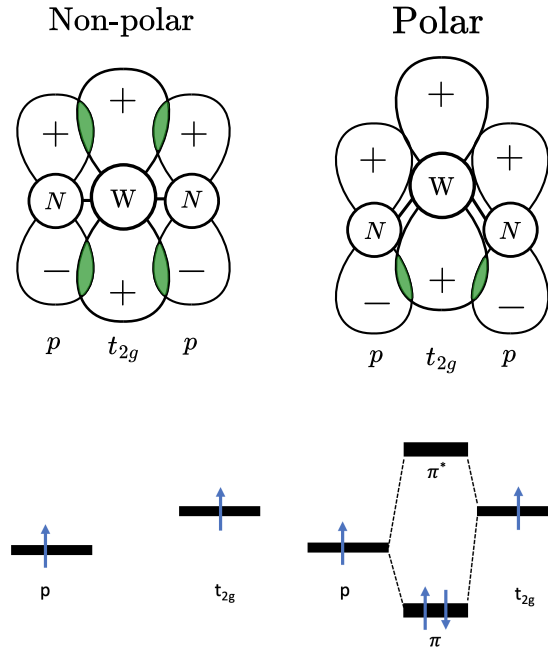
Figure 2.1: Illustration of the second order Jahn-Teller effect in $LaWN_3$, showing the orbital overlap and the resulting molecular orbital diagram.

3 Background

The sections on Perovskites and LaWN$_3$ are also included in the previous work[1], but have been rewritten and updated for this project.

3.1 Perovskites

Perovskites are a class of compounds with a general chemical formula of ABX$_3$ arranged in the perovskite crystal structure [12]. The prototypical perovskite is the $Pm\bar{3}m$ structure, with the B atom in the center of the X-octahedra and A atoms in the corners of the cubic unit cell, see Figure 3.1. The A and B atom are metallic cations while the X anion is non-metallic. Oxygen is the most common X element, but perovskites with halogens and pnictogens also exists. The different oxidation state in element X allows for different A and B cations to be used. The oxidation state of the metallic cation (A and B) allows for perovskites which do not follow the typical ABX$_3$ formula. As an example, $Ba_2Bi^{+3}Bi^{+5}O_6$ is a perovskite where the B atom, Bi, has two different oxidation states. Furthermore, each of the A and B atoms can be represent different elements in the same structure. The perovskite Ca_2CaUO_6 have calcium as both the A and B cation in the structure. The flexibility in compositional engineering is one of the advantages for perovskites.
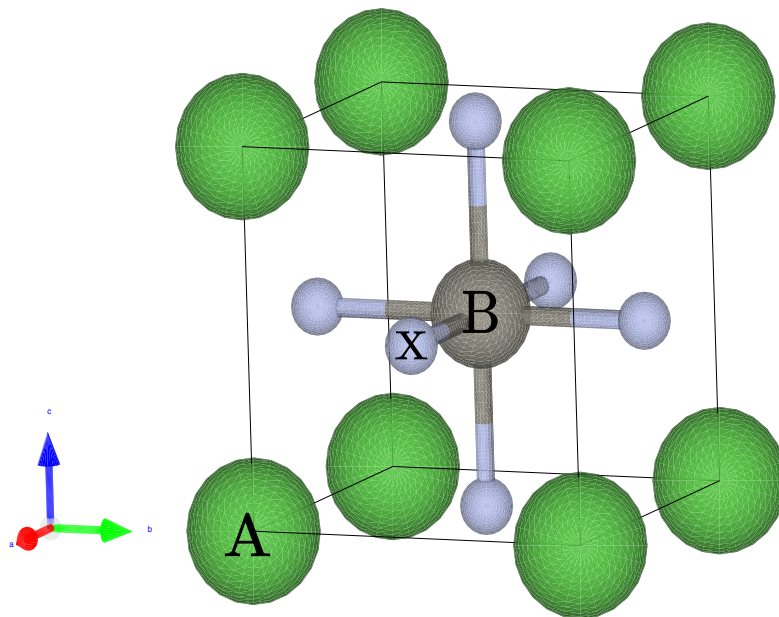
Figure 3.1: The prototypical perovskite cell belonging to the $Pm\bar{3}m$ space group, with A, B and X atoms marked. Prepared in VESTA [13].

The size relationship between the A and B is important for the functional properties of perovskites, where stress caused by the mismatch between the atom sizes can distort the crystal structure [14]. The mismatch in size of the atoms in perovskites

is described by Goldschmidt´s tolerance factor, t, given as

$$t = \frac{r_A + r_X}{\sqrt{2}(r_B + r_X)}, \tag{1}$$

where r_i is the radius of the atoms in the perovskite [15]. The tolerance factor can predict the distortions of the crystal structure in perovskites, given in Table 3.1. The distortion of the crystal structure can also involve atomic displacements or twisting and tilting of the octahedra, thus lowering the symmetry of the crystal structure. The tilting of octahedra in perovskites can be described by the Glazer notation. The octahedral tilt is described by the rotation around the Cartesian axes, using two parameters. The first is a letter, which specifies the rotation of octahedra around the specific axis, relative to the others. If the letters are all the same, the rotation angle is equal in all the Cartesian directions. The tilting direction of the adjacent layers of octahedra, is described by the second parameter, given in the superscript of the letter. A positive superscript gives a tilt in the same direction, while a negative give tilt in the opposite direction [16]. Due to the large flexibility in both elemental composition and crystal structure, perovskites can be engineered for many different applications such as solar cells, as ionic or electronic conductors and as ferroic materials [17]. As an example, the efficiency of perovskite solar cells has reached 25.2 %, rivaling the silicon based solar cells [18], showing the excellent properties of perovskites.

Table 3.1: Goldschmidt´s tolerance factor and resulting crystal structure [19]

Tollerance factor	Crystal structure
t>1.075	Hexagonal
1<t<1.075	Ideal cubic perovskite
0.86<t<1	Orthorhombic, rhombohedral or tetragonal
t<0.86	Other

In recent years, research have focused on halide perovskites due to the combination of good optoelectronic properties, flexibility in composition and low fabrication cost [20]. Organic-inorganic hybrid perovskites have shown huge potential for cheap and efficient photovoltaic devices, where also the dimensions of the material can be tailored to the specific devices [21]. In the search for new stable perovskites, high-throughput computational studies have been used to find candidates with useful properties [22][23]. From these studies, new perovskites have been found and synthesized. New materials include nitride perovskites like $CeMoN_3$, $CeWN_3$ and $LaWN_3$, which are rare earth transition metal perovskite nitrides. The advantage perovskite nitrides have over halide and oxide perovskites is the predicted higher mechanical and chemical stability, due to the stronger covalent bonds nitrogen form in the perovskites. The inertness of nitrogen creates challenges with synthesis of the materials, limiting the number of the available stable nitride perovskites [24]. Na et al. [25] found an improved model for the synthesis of nitrogen perovskites, where the nitrogen perovskites have two potential energy barriers compared to one for oxide perovskites, explaining why synthesis of nitrogen perovskites are more difficult than their oxide counterparts. Nitride perovskites have been predicted to have large piezoelectric response and low temperature for magnetic ordering [26].

3.2 LaWN$_3$

LaWN$_3$ is a ferroelectric perovskite nitride [27]. The tolerance factor for LaWN$_3$ is 0.941, resulting in a rhombohedral structure [28]. From computational studies, the $R3c$ space group is found to have the lowest energy and the structure is dynamically stable[28][29][30]. The $R3c$ structure differs from the $Pm\overline{3}m$ configuration by antiferrodistortic tilt of the nitrogen octahedra and the displacement of the tungsten atom from the center of the octahedra, denoted t, as well as the displacement of the lanthanum atom, denoted s, see Figure 3.2. The rhombohedral unit cell angle in LaWN$_3$ is 60.47 degrees [30]. For LaWN$_3$, the tilt of the octahedra is in the $a^- a^- a^-$ direction in the Glazer notation, meaning that the octahedral rotation is the same around all Cartesian axes, and tilting in the adjacent layers are in the opposite direction. The $R3c$ structure can be represented in the primitive rhombohedral unit cell or the conventional hexagonal unit cell [31]. LaWN$_3$ is a semiconductor with an indirect band gap of 1.7 eV [32]. LaWN$_3$ has a polarization of 61 μC/cm^2 [30]. The large polarization in the structure is in the [111] direction in the primitive unit cell and originates from the displacement of tungsten and lanthanum from their centrosymmetrical positions.
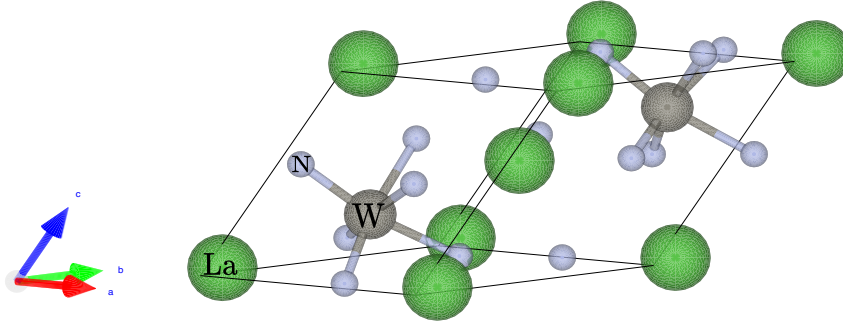
Figure 3.2: Primitive unit cell of LaWN$_3$ in the $R3c$ space group, with lanthanum shown in green, tungsten in gray and nitrogen in blue. Prepared in VESTA [13].

The majority of the work on LaWN$_3$ have been computational, due to the challenging synthesis of compound without a large number of defects. Liu et al. [28] found that the valence band maximum (VBM) and conduction band minimum (CBM) mostly consists of the La-d, W-d and N-p orbitals. They also found that LaWN$_3$ should exhibit a larger Young´s modulus than oxide perovskites like BiFeO$_3$ because of the stronger bonding in LaWN$_3$ [33]. Furthermore, LaWN$_3$ has a higher refractive index and dielectric constants than other perovskites considered in the study. Ren et al. [29] predicted that LaWN$_3$ has thermal conductivity which is comparable to common perovskite oxides BaTiO$_3$ and PbTiO$_3$. Geng and Xiao [34] investigated defects nitride perovskites, using LaWN$_3$ as the prototypical nitride perovskite. They found that vacancy of nitrogen atom has the lowest formation energy of the defects considered, but the high effective mass of the charge carriers would result

in lower conductivity compared to halide perovskites. Singh and Tripathi [35] investigated the possibility of doping $LaWN_3$ with strontium, which would enhance the optical properties of $LaWN_3$ significantly by lowering the effective mass of the charge carriers. Na et al. [25] predicted that tungsten could be doped with several different elements, giving a stable structure with composition $LaW_{1-x}B_xN_3$, where B could be Mo^{+6}, Os^{+6}, Po^{+6} and Ru^{+6}. Lai et. al [36] showed that the polar space group $Pna2_1$ of $LaWN_3$ has a large potential for photovoltaic applications, with a theoretical conversion efficiency of 32% found through spectroscopic limited maximum efficiency analysis, with the change in space group lowering the band gap to 1.36 eV.

Zhou et al. [37] was able to prepare oxygen free, bulk $LaWN_3$ through a high pressure and temperature reaction between $La_2W_2O_9$ and $NaNH_2$. The synthesized compound was confirmed to adopt the polar symmetry of $Pna2_1$. The difference from the ground state structure was explained by the amount of nitrogen vacancies which stabilizes $Pna2_1$ over the predicted ground state structure of $R3c$. The composition of the synthesized product was $LaWN_{2.6}$. $LaWN_3$ has also been synthesized as thin films with different deposition techniques. Talley et al. [38] was able to prepare oxygen free thin film $LaWN_3$ through ultra-high vacuum physical vapor deposition. From the thin film sample, they measured a strong piezoelectric response of 40 pm/V. Thin films of $LaWN_3$ was also found to be superconducting below 0.73K by Hanzawa and Hiramatsu, where the superconductivity was explained as a result of off-stoichiometry with deficiency of nitrogen and excess of tungsten [39].

3.3   Ferroics and Ferroelectricity

Ferroic materials have a non-disruptive phase transition resulting in spontaneous long-range ordering of an order parameter. The order parameter is switchable by external manipulation, like an external field [40]. For a ferromagnetic material, the order parameter is the magnetic moment which can be switched with an external magnetic field. The phase transition can be first order, discontinuous, or second order, continuous, and the transition temperature is called the Curie temperature, T_c [41]. Primary ferroics are ferroelastics, ferroelectrics, ferromagnetics and ferrotoroidics [42]. The primary ferroics are also described by the allowed symmetry operations in space and time, shown in Figure 3.3, characterizing the different types of ferroics. Primary ferroics are a direct consequence of the crystal symmetry in space and time. Ferroelectrics and ferromagnets does not have space inversion or time reversal symmetry respectively, ferroelastics have both types of symmetry, while ferrotoroidics have neither. A material that exhibits more than one primary ferroic ordering is known as a multiferroic [43].
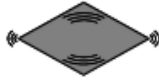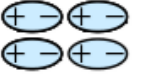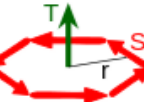
Figure 3.3: Overview over primary ferroics, with symmetry and order parameters describing the different ferroic materials [44].

Ferroelectrics have a phase transition from a non-polar to a polar state, where inversion symmetry is broken in the crystal structure. To break inversion symmetry, the crystal structure has to be noncentrosymmetric, resulting in a charge imbalance and therefore a polar moment in the structure. Of the 32 crystal classes, 21 are non-centrosymmetric, however not all noncentrosymmetric structures are ferroelectric. The polarization can be switched by an external electric field larger than the coercive field, E_c. When no field is applied, the polarization in the material is called the remnant polarization, P_R. Therefore, another characteristic feature of ferroelectrics is the hysteresis loop of the polarization when applying an electric field of different magnitude.

Traditionally, ferroelectrics have been used as capacitor and actuators, with $BaTiO_3$ being the text-book example of a ferroelectric material. The barium atom is displaced in the oxygen octahedra breaking inversion symmetry in the unit cell, see Figure 3.4.
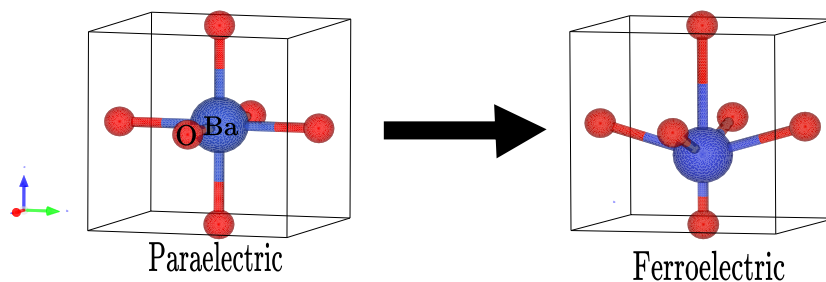
Figure 3.4: Transition between non-polar paraelectric state and polar ferroelectric state in $BaTiO_3$.

Modern applications of ferroelectrics are moving towards nanotechnology. Whether the phases and domains are stable at nanoscale and if the functional properties change when going nanosized are among the most important questions [45].

8

3.4 Domains and Domain walls

When the ferroic state emerges below the transition temperature, the order parameter orientates randomly throughout the structure. In a ferroelectric material, where the order parameter is the polarization, this will result in a randomization of the direction of the polarization throughout the structure, see Figure 3.5. A region where the ferroic order parameter is uniform is known as a ferroic domain. The domains form in order to minimize the energy of the system, but they also cost energy to form, resulting in a critical size of the domains where a single domain state can form [46]. The size of the domains in a material is determined by the trade-off between the cost of forming different domains and energy gain from depolarization of the material as well as anisotropic and elastic energies [47]. If a field larger than the coercive field is applied to the material, the domains align with the direction of the field.
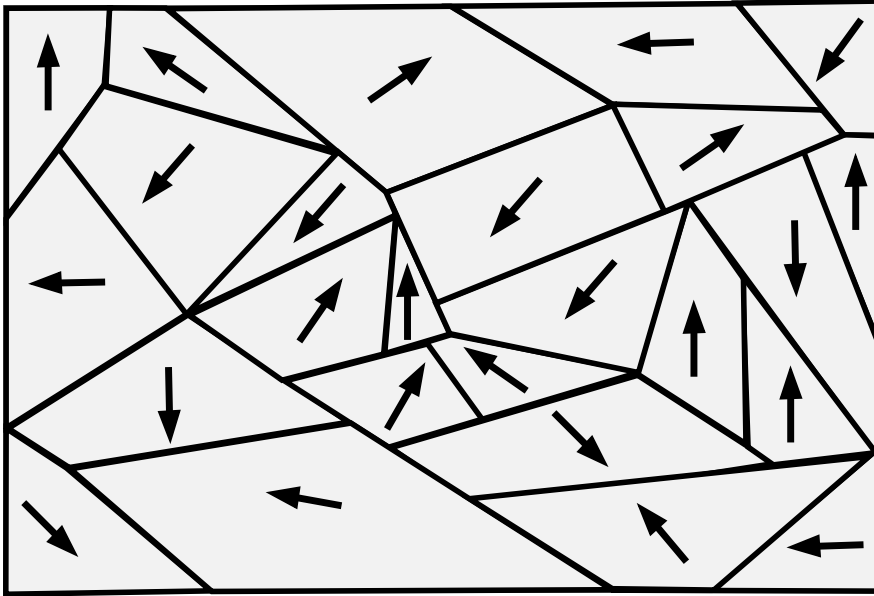
Figure 3.5: Ferroelectric material with random orientation of the polarization in the different domains.

The interface between two domains is called a domain wall (DW). In a ferroelectric DW, the polarization changes direction from one domain to the other. The possible DW configurations where the polarization is switched by 180° are parallel, head-to-head or tail-to-tail DWs, see Figure 3.6. The first type is known as neutral DWs, while the latter two are known as charged DWs. Ferroelastic DWs include a ferroelastic switching of the unit cell and switching of the order parameter. Rhombohedral ferroelectric DWs can therefore also have 71° or 109° DWs based on the geometry of the unit cell [48]. Ferroelastic transformation of the unit cell costs energy and can hence not be realized in all ferroic materials.
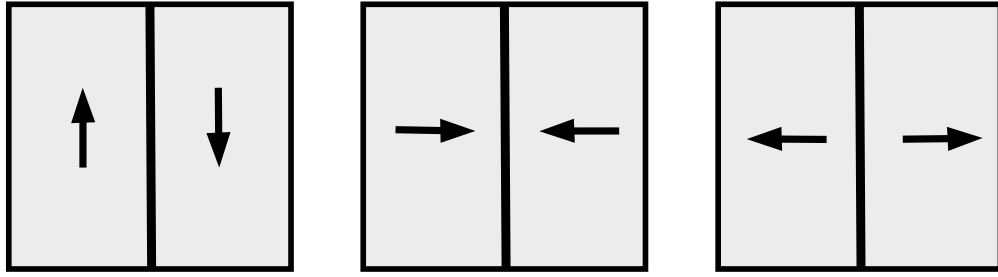
Figure 3.6: Illustration of parallel, head-to-head and tail-to-tail domain walls.

DWs can be classified by how order parameter switches in the DW. In a Bloch wall, the order parameter switches normal to the DW, while in a Néel wall it switches gradually in the direction of the domains, shown in Figure 3.7 [49].
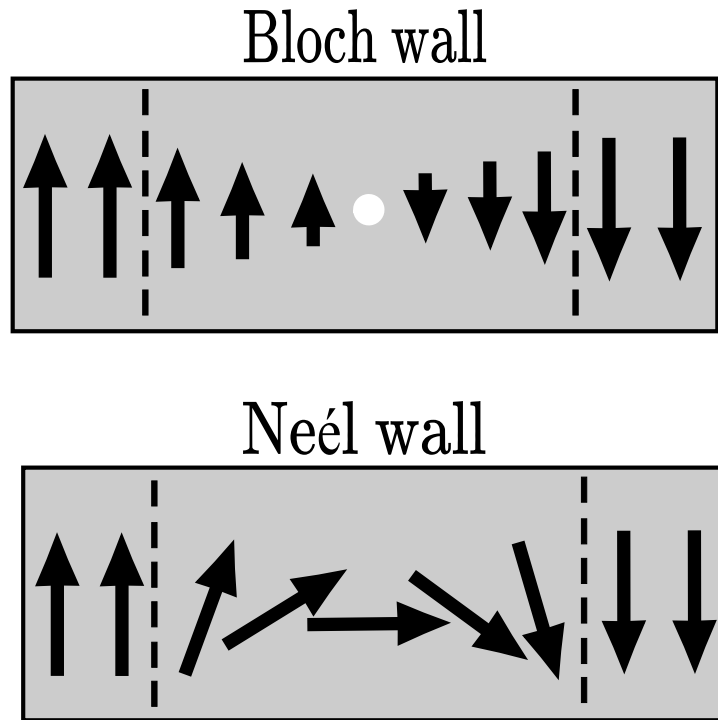
Figure 3.7: Illustration of the different switching of the order parameter in Bloch and Néel walls. The order parameter in the Bloch wall changes normal to the DW and gradually in the Neél wall.

3.4.1 Conductivity

As the crystal symmetry is different for the crystal in the domain and the domain wall, the domain wall can have different properties than the bulk phase, as described by Von Neumann's principle [50]. One example is the large difference in conductivity between bulk and domain wall in some materials. $LiNbO_3$ is a semiconductor with a large band gap, but domain walls in the structure have been observed to be conducting for single crystals [51]. The conductivity of ferroelectric domain walls have been explained by reduction in band gap, defects accumulating at the DW and shift in the band structure due to local electric fields [52]. The conductivity of a material is dependent on the amount of mobile charge carriers, p for holes, n for electrons and the mobility of the charge carriers, μ. For a material with both holes and electrons as charge carriers the conductivity can be expressed as

$$\sigma = qn\mu_e + qp\mu_h \tag{2}$$

where q is the elemental charge. The number of mobile charge carriers is dependent on the intrinsic number of charge carriers, the band structure of the material as well as the temperature. The number of mobile holes in a material at temperature T is

$$p = N_v exp(\frac{E_{vbm} - E_F}{k_B T}), \tag{3}$$

and the number of mobile electrons is described by

$$n = N_c exp(\frac{E_F - E_{cbm}}{k_B T}), \tag{4}$$

where E_F is the Fermi energy of the material, E_{vbm} is the energy of the VBM and E_{cbm} is the energy of the CBM. E_F in a semiconductor describes the energy difference between E_{cbm} and E_{vbm} in the material. The intrinsic number of electrons N_c and holes N_v are often increased in semiconductors through doping of the material. This increasing the number of mobile charge carriers, thus increasing the conductivity.

3.4.2 Domain Wall Motion

DWs are not static but move when external forces are applied to the domain structure. It has been shown that ferroelectric DWs can be nucleated at specific sites and that the propagation can be controlled [53]. This control over the domain structure of a ferroelectric material is important for ferroelectric memory devices like FeRAM or ferroelectric field transistors [7]. The domain wall mobility is dependent on the interaction between the DW and the defects in the structure and the position of the domain wall can be pinned by defects [54]. The migration barrier for DWs in $LiNbO_3$ is shown in Figure 3.8. The migration barrier for the DW is larger if the defects $Nb_{Li}^{\bullet\bullet\bullet\bullet}$ and V'_{La}, pinning the position of the DW. The Figure also shows the opposite effect for $Li_i^{\bullet}$ increasing the mobility of the DW. Defects can also promote

the formation of a higher energy domain wall in the structure. Defects in $LiTaO_3$ promotes the formation of a high-energy DW instead of the lowest energy DW [55].
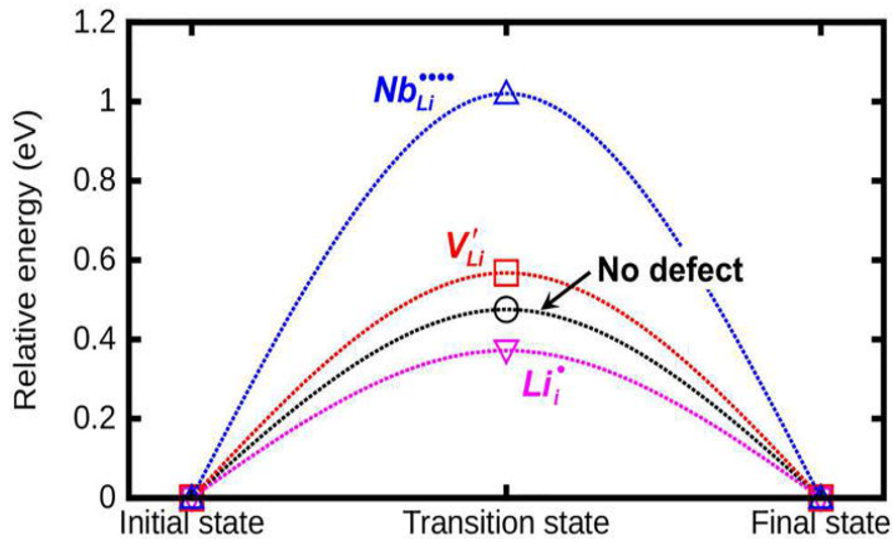
Figure 3.8: Migration barrier of DW in $LiNbO_3$ showing the influence different defects has on the DW [56]. The x-axis shows the position of the DW migrating from one equivalent position to the next, while the y-axis is the energy cost of moving the DW.

4 Theory

4.1 Quantum Mechanics

The Quantum Mechanics and Introduction to Density Functional Theory sections are based on my project thesis "Holes in the LaWN$_3$" [1] with some minor changes and additions.

The state of an electron is described by its wave function, ψ. The evolution of the wave function is given by

$$i\hbar\frac{d}{dt}\psi(\mathbf{r},t) = H\psi(\mathbf{r},t),\tag{5}$$

known as the Schrödinger equation (SE), where H is the Hamiltonian operator, i is the imaginary number and $\hbar$ is the reduced Planck´s constant. The Hamiltonian operator is dependent on the physical system and include both kinetic and potential energy terms. The time-dependent SE describes the evolution of the wave function, relating the energy, E, of the wave function with the Hamiltionian operator,

$$H\psi(\mathbf{r},t) = E\psi(\mathbf{r},t).\tag{6}$$

The energy solution to the SE is known as the eigenenergies of the electron, with the lowest energy solution being the ground state energy. A non-relativistic Hamiltionian for a single particle system is

$$H(\mathbf{r},t) = -\frac{\hbar}{2m}\nabla^2 + U(\mathbf{r},t),\tag{7}$$

where m is the mass of the particle, ∇^2 is the Laplacian operator and U is the potential energy of the particle as a function of space and time [57]. The first term of the Hamiltonian describes the kinetic energy of the particle and the second the potential energy. For static calculations, the time dependency of the SE can be ignored, resulting in the time-independent SE,

$$H\psi(\mathbf{r}) = E\psi(\mathbf{r}).\tag{8}$$

The probability of finding the electron at a position $\mathbf{r}$ is given by the modulus squared of the wave function

$$P(\mathbf{r}) = \psi^*(\mathbf{r})\psi(\mathbf{r}).\tag{9}$$

In most physical systems, an exact solution to the SE is impossible to obtain necessitating approximations to find the wave function. The Born-Oppenheimer approximation states, because of the large difference in mass between the nucleus and the electrons, the nucleus is stationary from the point of view of the electrons. As a result, the wave function of the system can be decoupled to the wave function of the electron and the wave function of the nucleus. Since the nuclei are stationary in the Born-Oppenheimer approximation, the terms for the nuclei in the Hamiltionian is a constant which can be ignored. For a system with more than one electron and

nuclei, the Hamiltionian describing the interaction between multiple electrons, i, and multiple nuclei is

$$H = [-\frac{\hbar}{2m} \sum_{i=1}^{N} \nabla_i^2 + \sum_{i=1}^{N} V(\mathbf{r}_i) + \sum_{i=1}^{N} \sum_{j<i} U(\mathbf{r}_i, \mathbf{r}_j)], \tag{10}$$

where V is the Coulombic attraction between the nuclei and electron and U is the Coulombic repulsion between the electrons in the system. The first term is the total kinetic energy of the electrons, the second is the attractive potential energy between an electron and a collection of nuclei, for all electrons i to N in the system and the last term is the repulsion between one electron and all the other electrons in the system. For independent particles, the total wave function of the system can be written as the product of the independent wave functions, known as the Hartree product. The total electron wave function is then

$$\psi(\mathbf{r}_1, ..., \mathbf{r}_N) = \psi_1(\mathbf{r})\psi_2(\mathbf{r}), ..., \psi_N(\mathbf{r}). \tag{11}$$

where $\psi_n(\mathbf{r})$ are the individual electron wave functions. The problem may be further simplified by considering the electron density rather than the full wave function of the system

$$n(\mathbf{r}) = 2 \sum_{i=1} P_i(\mathbf{r}), \tag{12}$$

where P_i is the probability density of electron i, reducing the problem to 3 spatial dimensions.

4.2   Density Functional Theory

Density functional theory (DFT) are calculations used to model a large variety of different materials and molecules[1]. DFT is used to model structures on an atomic scale, and the quantum mechanical behavior of the electrons and nuclei in the structure is therefore important. DFT calculations are static calculations on the wave function of the system. At 0K the energy of the structure is given as a functional of the electron density. This basis is used in DFT where the electron density rather than the wave function is used to solve the time-independent SE for the system.

4.2.1   Hohenberg-Kohn Theorems and Kohn-Sham Equation

DFT is built on two important theorems from Kohn and Hohenberg in the 1960s. First theorem states: *The ground-state energy from Schrödinger´s equation is a unique functional of the electron density*, meaning that if the ground-state electron density is known, the ground-state energy can be found through

$$E = E[n(\mathbf{r})], \tag{13}$$

---

[1]This introduction to Density Functional Theory was inspired by the book from Sholl and Steckel, Density Functional Theory: A practical introduction [58]

where $E[]$ is the energy functional relating the electron density to the energy in the system.

The second theorem states: *the electron density that minimizes the energy of the overall functional is the true electron density corresponding to the full solution of Schrödinger equation*, meaning if the total energy of the system is minimized, the correct electron density is found. It is important to note that the Hohenberg-Kohn theorem only holds for ground-state calculations.

Kohn and Sham realized that one can express the correct electron density as a set of single electron equations

$$[-\frac{\hbar}{2m}\nabla^2 + V(\mathbf{r}) + V_H(\mathbf{r}) + V_{XC}(\mathbf{r})]\psi_i(\mathbf{r}) = \varepsilon_i\psi_i(\mathbf{r}), \tag{14}$$

where V_H is the Hartree potential, V_{XC} is the exchange-correlation potential and ε is the energy of the single electron. This equation is known as the Kohn-Sham equation, where the nuclei are treated as stationary particles and the goal is to find the wave function for N-interacting electrons. The Hartree potential describes the interaction between the single electron at a position $\mathbf{r}$ and the electron density of the system, n at a position $\mathbf{r}'$ and is given by

$$V_H(\mathbf{r}) = e^2 \int \frac{n(\mathbf{r}')}{|\mathbf{r} - \mathbf{r}'|}d^3r'. \tag{15}$$

The total electron density of the system also includes the considered electron resulting in self-interaction, a limitation of using the Hartree potential. The exchange-correlation potential count for all the quantum mechanical effects which is not included in the other terms, and is defined as

$$V_{XC}(\mathbf{r}) = \frac{\delta E_{XC}(\mathbf{r})}{\delta n(\mathbf{r})}, \tag{16}$$

where E_{XC} is the exchange-correlation energy functional and δ denotes the functional derivative. This functional is nontrivial to describe accurate in general, except for a uniform electron gas where the electron density is constant for all points in space. DFT calculations uses a uniform electron gas model to approximate the exchange-correlation. Common approaches are the local density approximation, where the local electron density is used to find the exchange functional or the generalized gradient approximation (GGA) where the gradient of the electron density is also included. The exchange-correlation functional for GGA is

$$E_{XC}^{GGA} = \int d^3r e_X^{unif}(n(\mathbf{r}))F_{XC}(r_s(\mathbf{r}), s(\mathbf{r})) \tag{17}$$

where $e_x^{unif}(n)$ is the exchange energy for the uniform electron gas, s is the density gradient, r_s is the interelectronic distance and F_{XC} is the enhancement factor for the exchange-correlation in the specific GGA [59].

4.2.2 Solution Scheme

The electron density is found using the SE through a self-consistent scheme utilizing the two theorems from Hohenberg and Kohn, and the Kohn-Sham equation. First, a trial electron density is chosen. Then, the Kohn-Sham equation is used to find the single electron wave function. The wave function is then used to calculate the electron density. The new electron density is tested against the old one. If they are equal, then the correct electron density is found. If they are different, the old electron density is updated to the new one, and the process starts again until the scheme becomes self-consistent.

4.2.3 Bloch Function

The expansion of wave function in a periodic potential, like a crystal lattice, can be written as

$$\psi_{\mathbf{k}}(\mathbf{r}) = \exp(i\mathbf{k} \cdot \mathbf{r})u_{\mathbf{k}}(\mathbf{r}), \tag{18}$$

where $\mathbf{k}$ is the wave vector, $\exp(i\mathbf{k} \cdot \mathbf{r})$ is the phase of the wave function and $u_{\mathbf{k}}(\mathbf{r})$ is the lattice-periodic part of the wave function. Due to the periodicity of the potential, one can expand the wave function through a set of plane waves

$$u_{\mathbf{k}}(\mathbf{r}) = \sum_{\mathbf{G}} c_{\mathbf{G}} \exp[i\mathbf{G} \cdot \mathbf{r}], \tag{19}$$

where $\mathbf{G}$ is the reciprocal lattice vector. This expansion introduces the concept of reciprocal space, which is the Fourier transform of real space. An aspect of the transformation between real space and reciprocal space, is that long vectors in real space become short in reciprocal space and *vice versa*. The primitive unit cell in real space is called the first Brillouin Zone in reciprocal space, shown for a rhombohedral unit cell in Figure 4.1.
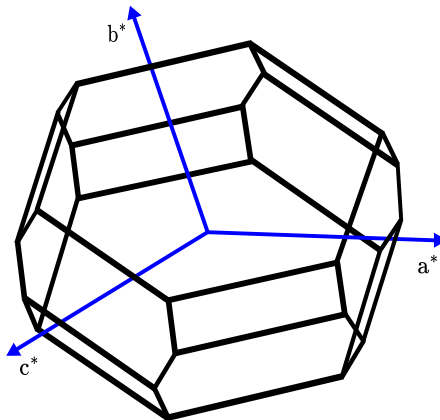
Figure 4.1: Brillouin zone of a rhombohedral unit cell inspired by Dual et. al [60]. The reciprocal space unit vectors are a*, b* and c*.

The total wave function can then be found by combining Eq. 18 and 19,

$$\psi_{\mathbf{k}}(\mathbf{r}) = \sum_{\mathbf{G}} c_{\mathbf{G}+\mathbf{k}} \exp[i(\mathbf{G}+\mathbf{k})\mathbf{r}]. \tag{20}$$

4.2.4 Energy Cutoff

As the Bloch functions can be written as a infinite sum of the periodic part of the wave function, a cutoff energy for the plane wave expansion in reciprocal space is introduced to minimize the computational time for the DFT calculations. Because low energy solutions of the SE are more physically important than high energy solutions, a cutoff energy is introduced

$$E_{cut} = \frac{\hbar}{2m}\mathbf{G}_{cut}^2, \tag{21}$$

which limits the infinite sum in Eq. 20,

$$\psi_{\mathbf{k}}(\mathbf{r}) = \sum_{|\mathbf{G}+\mathbf{k}|<G_{cut}} c_{\mathbf{G}+\mathbf{k}} \exp[i(\mathbf{G}+\mathbf{k})\mathbf{r}]. \tag{22}$$

The energy cutoff is found through convergence tests with a convergence criterion for the energy of the system. Once the change in energy is lower than the convergence criteria, the optimal energy cutoff has been found for the calculations.

4.2.5 k-Points

In DFT calculations, integrals over the first Brillouin zone with periodic boundary conditions are commonly used to evaluate the properties of the structure. To solve the integrals numerically, the integral is approximated to the sum over a set of points in the first Brillouin zone, called k-points. As real space is split in order to numerically integrate a function over $\mathbf{r}$, the function over a set of k-points in reciprocal space is evaluated. The numerical integral over the first Brillouin zone will converge towards the true value as the number of integration points increase, but at a computational cost. A convergence test for k-points is done where the change in total energy of the structure is evaluated, to minimize computational time while still giving accurate results.

4.2.6 Pseudopotentials

Most of the chemical properties of the atoms originate from the valence electrons, and the inner electrons are usually ignored. To ease the computational cost, pseudopotentials are used to approximate the inner electrons and only the wave function of the valence electrons are calculated. This in known as the frozen core approach [61].

4.2.7 Functionals

The generalized gradient approximation functional, "Perdew, Burke and Ernzerhof revisited for solids"(PBEsol), was used for all calculations in this project. PBEsol is a functional that minimizes the errors in surface energy produced by PBE [59].

4.2.8 VASP

For this project Vienna Ab-initio Simulation Package(VASP)[62] was used for the DFT calculations. VASP is a first principle program for atomic scale modelling. The code uses plane-wave pseudopotential for the DFT calculations.

4.3 Defects Calculations in DFT

Defects are imperfections in the crystal structure and can strongly influence the properties of the material. An imperfection in the crystal lattice with at least one of its dimensions being on the order of the diameter of the atoms in the structure is called a crystalline defect. A point defect is a crystalline defect which is connected to specific atomic positions in the crystal. A vacancy of an atom in the structure, or an interstitial placed atom are typical point defects in a ceramic material, together with antisite atomic placements. Antisite defect is when one species of atom is placed in the position of another species in the crystal. Vacancy of an atom A in the structure is denoted V_A and the antisite placement of atom A in the position of atom B is denoted A_B. Using the Kröger-Vink notation, a positively charged vacancy of atom A is shown in the superscript $V_A^{\bullet}$ while the negatively charge vacancy is V_A' [63]. These charges need to be compensated with electrons, holes or other defects to ensure charge neutrality in the material. In ceramics the anion is often relatively large compared to the cation and is therefore unlikely to be in the interstitial position compared to the cation [64].

Defects in the structure can drastically change the properties of the material, hence introduction of defects are commonly used to modulate the properties of the material. One of these methods is doping, which is used to increase the conductivity of semiconductors. DFT calculations of defects can give valuable, theoretical insights in how defects effect the material, and the concentration of the defects that can be expected.

4.3.1 Chemical Potential Diagram

The chemical potential diagram shows for which chemical potentials the different phases are favourable, similar to a phase diagram. The chemical potentials, denoted μ, are calculated from the energy of the pure elements as well as the energy of competing phases. The result is a 3D-diagram using the chemical potential of the pure elements as axes, providing the "volume" where the different phases are favorable, see Figure 4.2, where the chemical potential diagram for the combination of La,

Ga and O is shown. The pink area shows the chemical potentials where LiGaO$_2$ is favourable to form, with competing phases in blue. The gray area shows typical synthesis conditions, which is often included in the chemical potential diagram. With this diagram one can find the conditions needed for synthesis of the different phases.
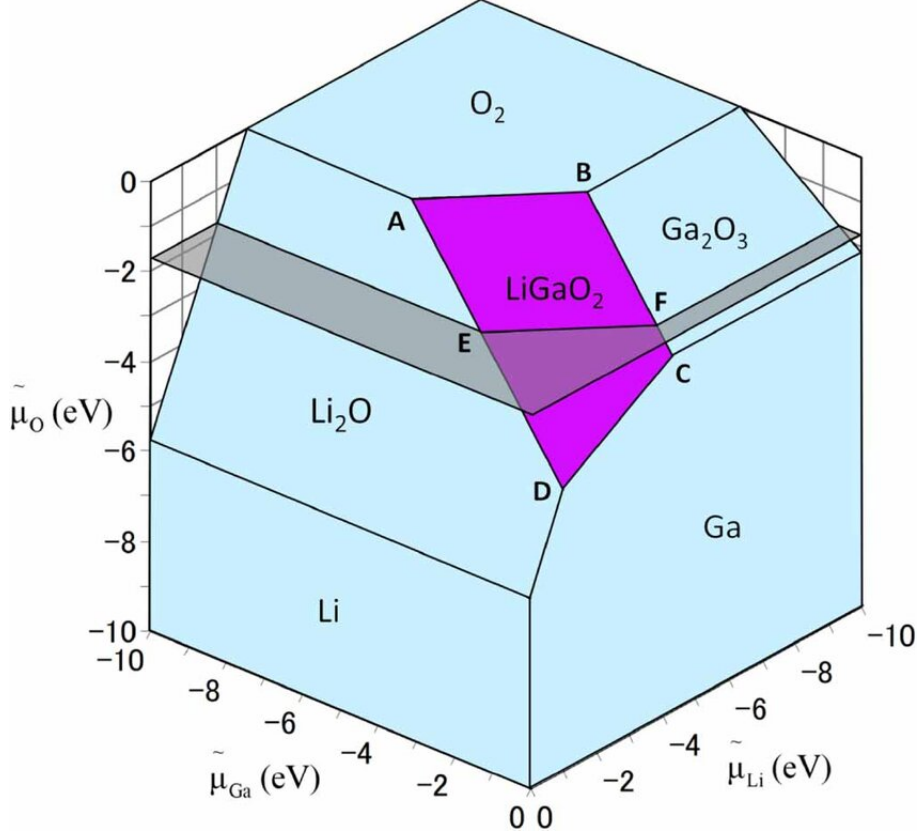
Figure 4.2: Chemical potential diagram for LiGaO$_2$ from Dabsamut et. al [65]. The pink area shows for which chemical potentials of O, Ga and Li LiGaO$_2$ favorable, and the gray area shows typical synthesis conditions for O$_2$.

Using the ideal gas model the chemical potential of a gas, i, depends on temperature and partial pressure, p, of the gas can be written as

$$\mu_i(T, p_i) = \mu_i^0 + \frac{1}{2}k_b T \ln(p_i), \tag{23}$$

where μ_i^0 is the chemical potential in the reference state. In this equation the chemical potential in the reference state is assumed to be independent on temperature. The DFT total energy calculation of the bulk elements is typically used for the chemical potential in the reference state, but this is known to be inaccurate [66].

4.3.2 Defect Formation Energy

Calculations of formation energy of defects can indicate which defects that can be expected in the material and the concentration of defects. For DFT calculations the defect formation energy of a defect in a cell with net charge q is

$$\Delta H_f(D, q) = E_D(q) - E_H + \sum_i n_i(E_i + \mu_i) + q(E_f + E_{vbm} + E_{corr}^{pot}) + q^2 E_{corr}^{IC} + E_{corr}^{BF},$$

(24)

where E_D is the energy of the defect cell with charge q, E_H is the energy of the perfect host cell. If atom i was removed, n is 1, or if the atom was added, n is -1. The energy and chemical potential of atom i is E_i and μ_i, respectively. E_{corr}^{pot} corrects for the change in the VBM in the defect cell from the host cell, known as the potential alignment correction. E_{corr}^{IC} is the image charge correction which corrects for the fictive electrostatic interaction in a charged cell, due to periodic boundary condition of the simulation. The band filling correction, E_{corr}^{BF}, is the correction for band filling of shallow defect levels due to the large concentration of defects in the structure [67]. The potential alignment correction is given as the difference in potential for the atoms in the defect cell with charge q, $V_{D,q}$ and in the host cell V_H. The image charge correction is dependent on the size of the defect cell used for calculations and the dielectric constant of the material. Band filling correction depends on the k-points used, the occupancy of the band, the band energies and the CBM for donor defects or VBM for acceptor defects after correcting for potential alignment of the defect cell [68].

It is important to note that these defects are calculated at the dilute limit and kinetics are not considered. Thus, the results only indicate the formation energy of the different defects. A negative formation energy does not mean that the material is unstable and will spontaneously disintegrate.

4.3.3 Transition Level Diagram

To understand the effect the defects have on the Fermi energy and the concentration of defects, a transition level diagram can be constructed. The diagram is constructed using Eq. 24 to calculate the defect formation energy as a function of the Fermi energy, see Figure 4.3. For the differently charged defects, the defect with the lowest formation energy is included. The Fermi energy where a defect with charge q and the same defect with charge q' has the same formation energy is called the transition level of the defect. If the transition level is far from the band edges it is called a deep defect, while if the transition level is close to the band edges or inside the band, it is called a shallow defect. All the charges from the defects need to be compensated, either by defects with opposite charge, or by charge carriers, electrons or holes. When all relevant defects are included in the diagram, the Fermi level can be found by locating the intersection point between the different defect formation energies. A positive defect adds electrons to the structure, a donor defect, while a negative defect adds holes to the structure, an acceptor defect.

Transition level diagram
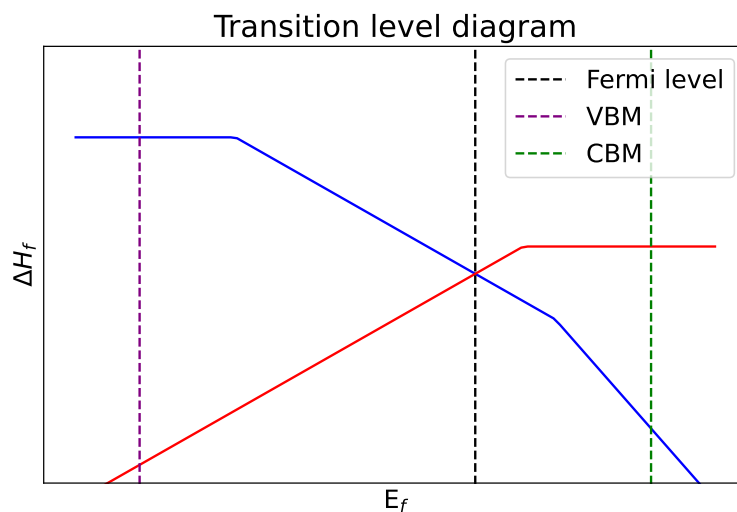
Figure 4.3: Illustration of a transition level diagram. The acceptor defect is blue and the donor defect is red. The intersection point gives the Fermi level. The VBM and CBM is material dependent and does not change with the defect.

4.4 Nudged Elastic Band

Nudged elastic band (NEB) is an approach to locate the minimum energy path between two states or between reactants and products in a reaction. Intermediate images between the initial and final state are created. By optimizing intermediate images and connecting springs between the images, the lowest energy path can be found. Climbing image NEB is a modification to NEB, which ensures one image at the saddle point of the minimum energy path in order to accurately find the energy barrier between the two states [69][70].

5 Computational Method

For all calculations a plane-wave cutoff value of 550 eV, and a k-point grid of 0.2726 in fractional cell units or denser, was used. The values were found as described in my project thesis through convergence tests [1].

The $R3c$ structure was optimized with a force criterion on the atoms of less than 0.1 meV/Å^2. The optimized primitive structure was used to make the conventional cell for subsequent calculations. With the primitive and conventional cell, different bulk reference values were found, shown in Table 5.1, where t displacement of the tungsten atom in the nitrogen octahedra and s is the displacement of lanthanum from the centrosymmetrical position [71]. Due to the displacement of the tungsten atom, the structure has one short and one long tungsten-nitrogen bond. The polarization, **p**, in the structure was found by comparing the polar $R3c$ structure with the non-polar $R\bar{3}c$ structure using the point charge model. The parameters θ and ϕ describe the in-plane and out-of-plane W-N-W angle.

Table 5.1: Bulk properties of LaWN$_3$ found through structural optimization of the $R3c$ space group [1].

t	0.2336 Å
s	0.2174 Å
W-N	1.903 Å, 2.146 Å
p	52.41 μC/cm^2
θ	159.57°
ϕ	159.57°

5.1 Domain Walls

The X- and Y-walls were found using the symmetries of the optimized $R3c$ structure, see Figure 5.1. The symmetry plane for the X-wall is $(\overline{1}2\overline{1})$ while for the Y-wall the symmetry plane is $(\overline{1}10)$. For the construction of the DW, the conventional unit cell was used for the X-DW, while for the Y-wall the primitive unit cell was used. The unit cell of the X-DW has 30 atoms, while the unit cell for the Y-DW has 20 atoms with different unit cell parameters, see Table 5.2. The 180° DWs were made for both X- and Y-domains by flipping the polarization direction 180° through the supercell. Both the 71° and 109° DWs were made for the Y-domain using an optimized pseudocubic $R3c$ structure with cell angles equal to 60°, see Figure 5.2. Supercells of size 1x1x2, 1x1x4, 1x1x6 for the X-DW and 1x1x2, 1x1x4, 1x1x6, 1x1x8 for the smaller unit cell of the Y-walls were made.
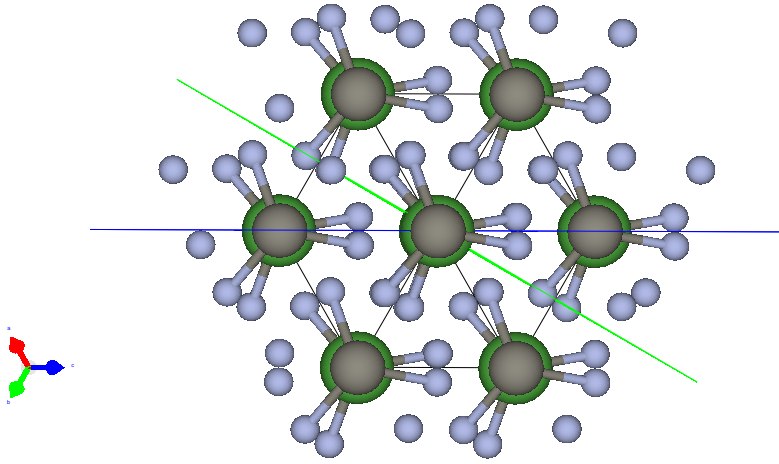
Figure 5.1: Different domain symmetries in the primitive cells. Blue plane shows the symmetry in the Y-domain and green plane is the X-domain. Prepared in VESTA [13].

Table 5.2: Unit cell parameters used to create the different DW supercells.

Cell type	a	b	c	α	β	γ
Primitive	5.61938	5.61938	5.61938	60.3780	60.3780	60.3780
Conventional	5.65143	5.65143	13.72349	90	90	120
Pseudocubic	5.61938	5.61938	5.61938	60	60	60
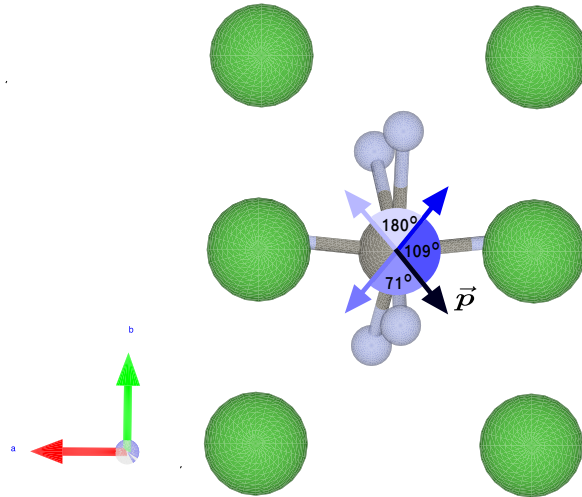
Figure 5.2: The different directions for the polarization in Y-walls, with the displacement of tungsten (gray) in the nitrogen ocahedra (blue) and lanthanum (green) on the sides of the "unit cell". Prepared in VESTA [13].

5.1.1 Structural Optimization

The different DW supercells were optimized to a force criteria of 0.03 eV/Å. The supercells have two DWs, one in the middle of the cell and one on each end. The end domain walls are the same wall because of periodic boundary conditions. A convergence test for the DW energies was used to establish the optimal length of the supercell used for further calculations. The cost of forming a DW, where the polarization switches direction, is called the DW formation energy and is given in energy per area. For the smaller supercells, 1x1x2 and 1x1x4, the structure took a single domain state upon optimization, hence no value for the DW formation energy could be calculated. For all calculations, the largest supercell of the DW was used.

5.1.2 Structural Parameters

The change in W-N bond length, the angle W-N-W angle and the polarization were followed through the DWs. As the tungsten has three short and three long nitrogen bonds, because of the displacement from the center of the nitrogen octahedra, the average short and long bond length was found for each tungsten atom. The W-N-W angles were separated into in-plane and out-of-plane angles with respect to the DW, see Figure 5.3.
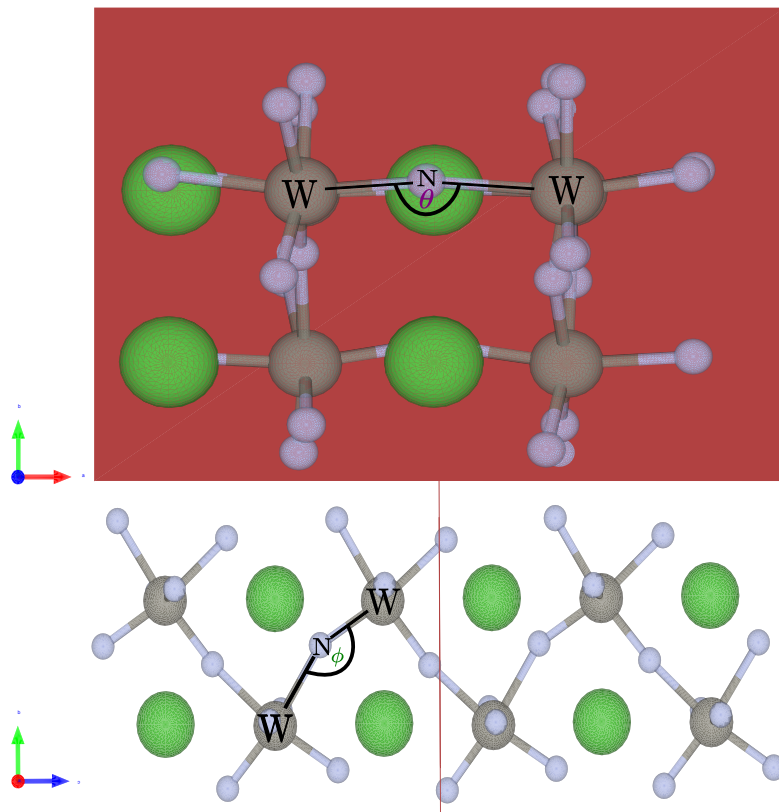
Figure 5.3: Definition of the in-plane θ, (above) and out-of-plane ϕ, (below) W-N-W bond angles in the constructed Y-DW supercells. Prepared in VESTA [13].

For the calculations of the polarization, a non-polar reference supercell without a DW was made and the displacement of each atom in the different DWs was found. The total polarization was then calculated through

$$\mathbf{p} = \frac{1}{\Omega} \sum_i q_i \mathbf{r}_i, \tag{25}$$

where Ω is the unit cell volume, q_i is the charge and $\mathbf{r}_i$ is the displacement of atom i. The 1x1x8 Y-DW supercells consists of 16 cells with 2 formula unit each. The point charge model was used for the calculation and the formal charge was used for the charges, $q_{La}=+3$, $q_W=+6$ and $q_N=-3$ with the elementary charge as the unit value.

5.1.3 Density of States

To investigate the electrical properties of the DW, the density of states (DoS) was calculated for the different DWs. DoS, $g(E)$, is the number of states per energy of the system, as a function of energy and defines

$$g(E)\Delta E := \text{number of states with energy between } E \text{ and } E+\Delta E$$

To compare with bulk values, DoS for $R3m$ and $R\bar{3}c$ were calculated. The $R3m$ is the polar rhombohedral structure without the rotation of the octahedra, and the $R\bar{3}c$ is the non-polar rhombohedral structure with octahedral rotation. These structures were first optimized to a force criterion of 0.01 eV/Å^2.

To see the evolution of the DoS in the supercells, layer-resolved DoS was used, showing the contribution to the DoS for each atom in the structure. Because of the expected lower band gap in the domain walls, gaussian smearing was used for the DOS calculations.

5.2 Defects

5.2.1 Chemical Potential Diagram

To construct the chemical potential diagram of $LaWN_3$ the program *CPLAP* was used [72]. The program uses formation enthalpy for competing phases and $LaWN_3$, to construct the diagram. The competing phases used for the calculations was LaN and WN_2 and pure elements used to calculate the formation enthalpy were La, W, and N_2, shown in Table A.1. Except for oxygen, the energy of these phases was found in my project thesis [1], where different space groups of the competing phases were optimized, and the lowest energy configuration was used to calculate the formation energy of the compounds.

5.2.2 Defect Formation Energy

To calculate the defect formation energy, a 2x2x1 supercell of the conventional cell containing 120 atoms was structurally optimized and used for the defect calculations. It is important to have a large enough supercell to make sure that the defect does not interact with itself through the periodic boundary conditions. The supercell size was confirmed to be large enough by plotting the displacement of the atoms in the defect supercell, which was around 0.2 Å for most atoms, see Figure B.1, B.2, B.3 and B.4.

The point defects calculated were La and N vacancies, as well as antisite La and W, where La_W is lanthanum in a tungsten site and W_{La} is tungsten in a lanthanum site. The defects considered were found to be the dominating by Geng and Xiao [34]. Oxygen substitution of nitrogen was also considered because of the problem with oxygen contamination during synthesis. The chemical potential of oxygen was calculated with Eq. (23), with oxygen rich conditions having a partial pressure of 0.2 and oxygen poor conditions having a partial pressure of 10^{-8}. Since all elements in the structure only have one Wickoff site, the atomic positions are equal, thus the position of the defect in the supercell does not matter. The energy of the pure elements was calculated in my project thesis and used further in the calculations [1].

All defects were calculated for differently charged and neutral cells. To make the vacancies, the specific atom was removed from the structure and the structure was optimized structurally with respect to the atomic positions. For antisite defects, one atom was replaced by a different atom, and the structure was optimized. The defect structures were optimized structurally to a force criterion of 0.03 eV/Å^2. For the negative charged cells, electrons were added to the neutral cell, while for positive charged cells electrons were removed. A vacancy of nitrogen with charge $+3q$ is denoted $V_N^{\bullet\bullet\bullet}$ and will result in a neutral cell, while a vacancy with no charge is denoted $V_N^{\times}$ and will result in a cell charge of 3q. The chemical reaction in the two cases are

$$N_N^{\times} \rightarrow V_N^{\bullet\bullet\bullet} + \frac{1}{2}N_2(g) + 3e^-, \tag{26}$$
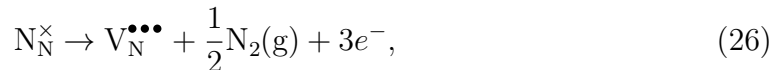
The removal of the nitrogen atom is compensated with three electrons, resulting in a neutral cell. For the neutral defect however, the reaction becomes

$$N_N^{\times} \rightarrow V_N^{\times} + \frac{1}{2}N_2(g), \tag{27}$$
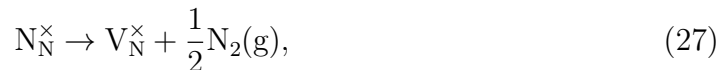
where the charge from the nitrogen vacancy is no longer compensated, resulting in a charged cell. This charge needs to be compensated to have a charge neutral structure by charge carriers or other defects.

For all defect cells band filling, image charge and potential corrections were calculated for the different charged and neutral cells. The band filling and potential alignment corrections were calculated with the methods from Lany and Zunger [67]. The image charge correction was calculated for the defect supercell, using the dimensions of the conventional cell and the dielectric tensor of LaWN$_3$, with the method from Murphy and Hine [73]. The total static dielectric tensor, ε_{ij}^0, was calculated for bulk $R3c$ LaWN$_3$ in the previous work [1] and is shown in A.1. The resulting defect supercell energies and corrections are shown in Table B.1 and B.2.

5.2.3 NEB for Defect Mobility

Climbing image NEB was used to find the migration barrier for vacancies in the structure. Both V_N and V_{La} were moved to a neighbouring site, and an atom was placed in the old vacancy position before the structure was optimized. Linear interpolation was done to create five images between the initial and final position of the vacancy and optimized with springs between the images. These images were optimized structurally to a force criterion of 0.03 eV/Å, with a spring constant of -5 eV/Å. The energy difference from the initial state gives the migration barrier of the defect. The migration barrier was calculated for cell with neutral charge and for cells with $|q|=3$ to see the effect of the cell charge.

6 Results

6.1 Domain Walls

6.1.1 Formation Energy

The formation energy for the different types of DW in LaWN$_3$ is shown in Table 6.1. The 71° DW has the lowest formation energy and the 109° DW has highest formation energy of the DWs. The two 180° DWs have similar formation energy, with the Y-type DW having a slightly lower formation energy than the X-type. Therefore, no further calculations were done on the X-type 180° DW.

Table 6.1: Formation energy of different domain walls in LaWN$_3$.

Type	Energy/Formation energy [meV/Å^2]
71°	5.01
109°	15.65
180°-Y	13.45
180°-X	13.59

6.1.2 W-N Bond Length

Figure 6.1 shows the evolution of the average tungsten-nitrogen bond length throughout the long axis of the supercells. As the unit cell for the Y-DW contains two tungsten atoms, there are two long and two short bond lengths in the Figure. For all DW supercells, bulk values for the bond length are reached in the middle of the domains and deviates progressively upon approaching the middle of the DW. The Figure also shows drift in the structure for the Y-DW with the long and short bond length not matching for the two tungsten atoms. The drift can be explained by small deviations in the position of the atoms in the two different domains and a flat energy landscape. The supercells were made by combining two domains with different polarization directions, and small differences in atomic positions exists in the two domains. When optimizing the structure, the forces on the atoms are different because of the unequal positions and will therefore be moved differently. The energy landscape is very flat for the DWs and the position of the atoms is therefore updated many times in order to reach the force criterion. Small differences in the forces on the atoms will result in a large drift in the position of equivalent atoms.
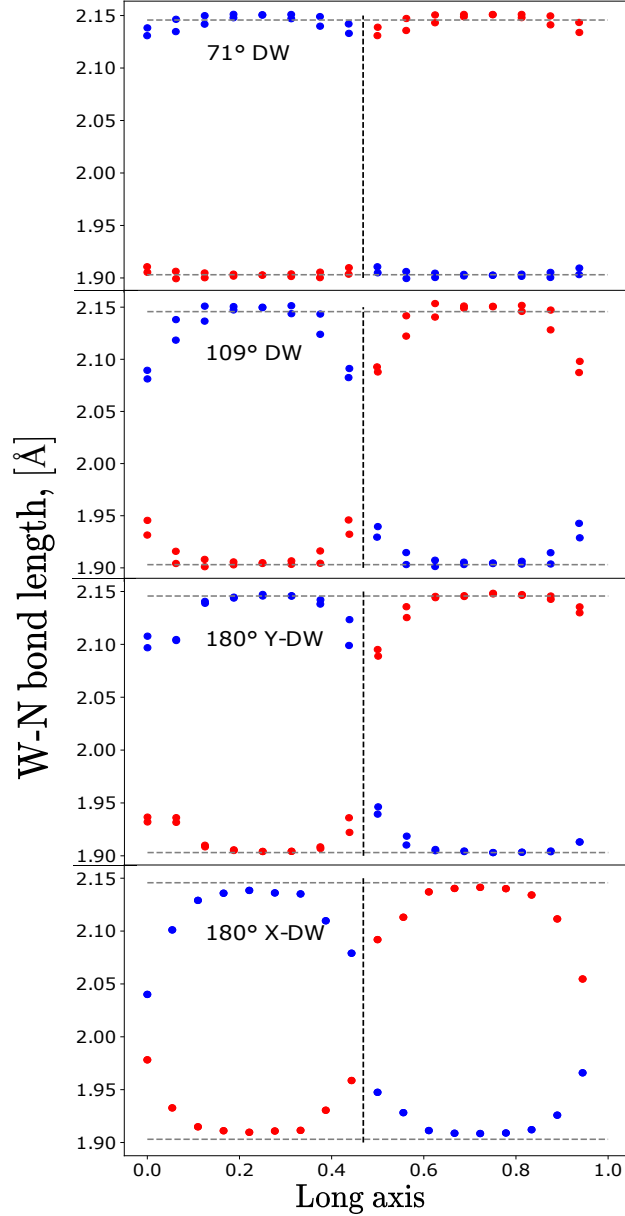
Figure 6.1: Average short and long W-N bond lengths along of the long axis, given in fractional coordinates, of the different supercells. The vertical dashed black line indicates the middle of the DW and the horizontal dashed gray lines indicate the bulk values.

The largest deviation in bond lengths is found in the middle of the DW with bulk values furthest from the DW. The 71° DW has a much lower degree of distortion in the bond lengths than the other types of DW. For the 71° DW, the long bond lengths have a maximum distortion of 0.69% and the short bond lengths have 0.4%. The maximum distortion in the 109° DW is 3.01% for the long bond lengths and 2.25% for the short bond lengths, while for the 180° Y-DW the bond length distortions are 2.65% and 2.27%, respectively. For the 180° X-DW the long bonds are 4.92% distorted while the short is 3.95% distorted, the largest degree of distortion of the DWs.

6.1.3 W-N-W Angle

The change in the in-plane angle, θ, and the out-of-plane angle, ϕ, of the W-N-W bonds is plotted along the long axis of the Y-supercells in Figure 6.2. The drift of atoms can again be seen as the out-of-plane angles split in two, with one angle becoming larger and one smaller than the bulk value for equivalent tungsten atoms in the structure. The Figure shows a larger spread in angles in the 71° DW than for the 109° DW and much larger than the 180° DW. The Figure also shows the largest deviation from bulk values in the middle of the DW, and values approaching bulk in the middle of the domains. The spread for W-N-W bond angle is smallest for the 180° DW.
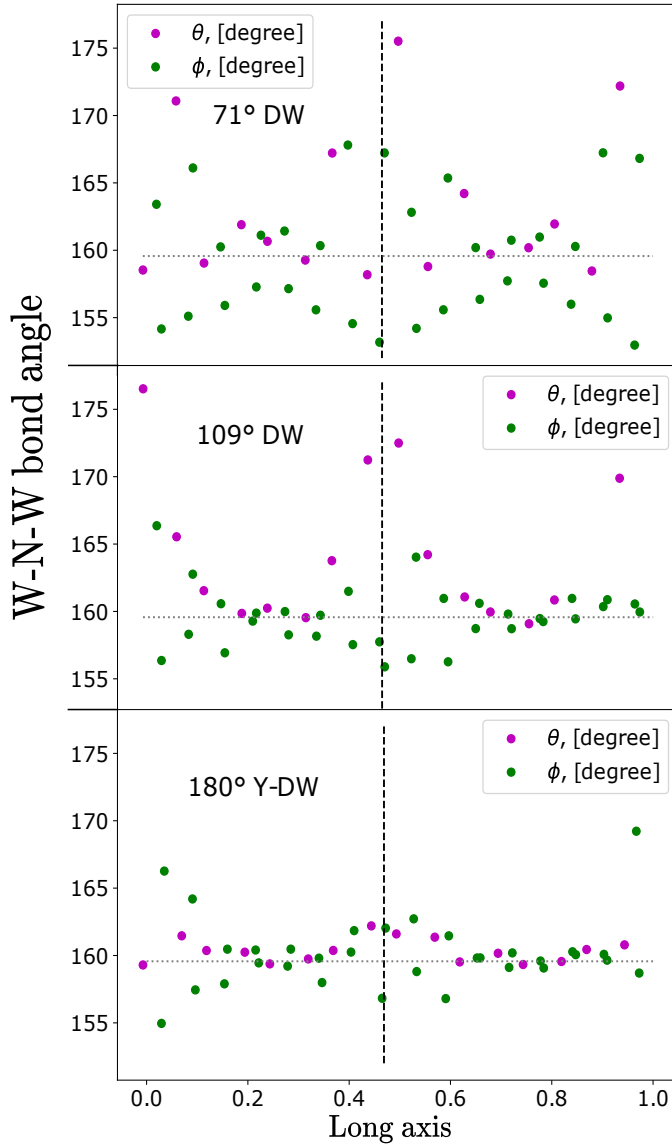
Figure 6.2: The W-N-W, θ and ϕ, along the long axis of the supercell, given in fractional coordinates, for different types of DW. The dashed vertical line shows the middle of the DW, the horizontal line, shows the bulk value for the bond angles.

6.1.4 Polarization

The evolutions of the polarization for the different DWs are shown in Figure 6.3. The polarization shows the same trend as the W-N bond lengths, where the largest deviation from bulk values is in the 180° Y-DW and the smallest deviations are in the 71° DW. In the 180° Y-DW the polarization in the middle of the DW is more than 20 μC/cm^2 lower than the bulk value in the middle of the domain. The fact that the polarization is not reaching bulk values in the flipped domain can be attributed to the domains not being large enough in the simulation.
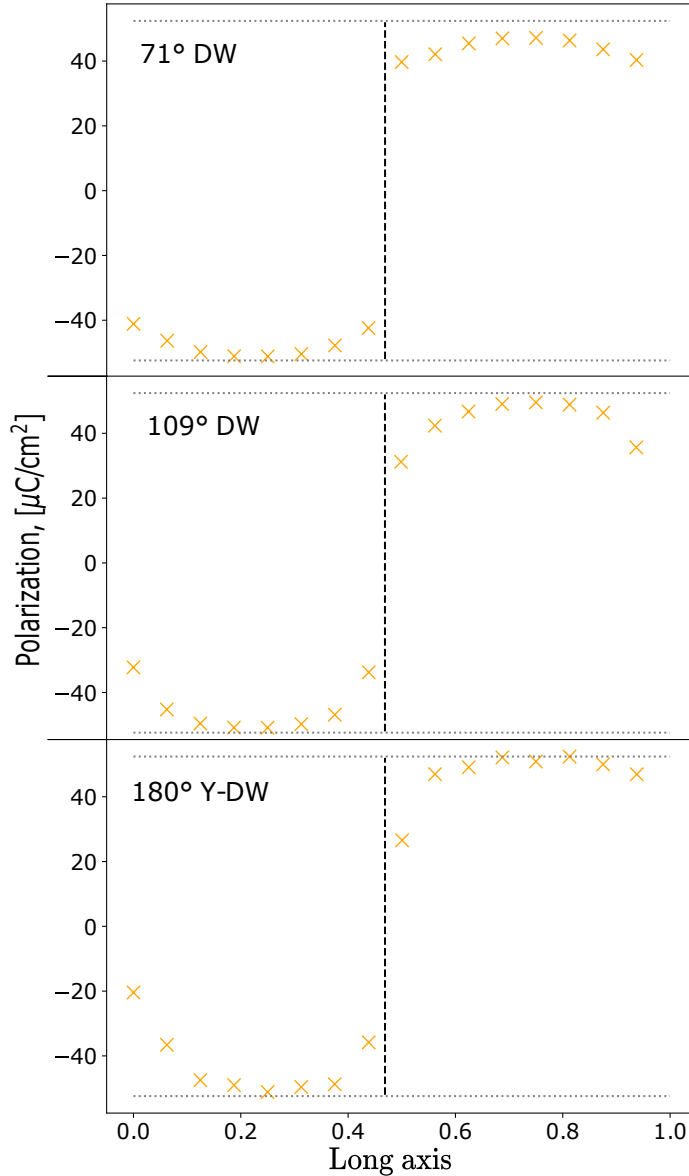
Figure 6.3: Polarization across the different domain walls along the long axis of the supercell, given in fractional coordinates. The dotted gray line shows the bulk polarization and the black dashed line shows the middle of the DW.

6.1.5 Bulk DoS

The DoS of the VBM and CBM for both the $R3m$ and $R\overline{3}c$ space group in the bulk state is shown in Figure 6.4. The band gap for the $R3m$ structure of LaWN$_3$ is 0.3 eV while the $R\overline{3}c$ has no band gap, showing a metallic DoS. The CBM for the $R3m$, shown in Figure 6.4a, is flat around the minimum value with a peak at 1 eV, and W$_d$ has the greatest contribution to the DoS in the conduction band. For the $R\overline{3}c$ structure, the conduction band has two large peaks at energies close to the Fermi energy. The peaks consist of the nitrogen p- and tungsten d-orbital. For both structures the VBM is dominated by the nitrogen p-orbital.

(a) DoS for $R3m$.   (b) DoS for $R\overline{3}c$
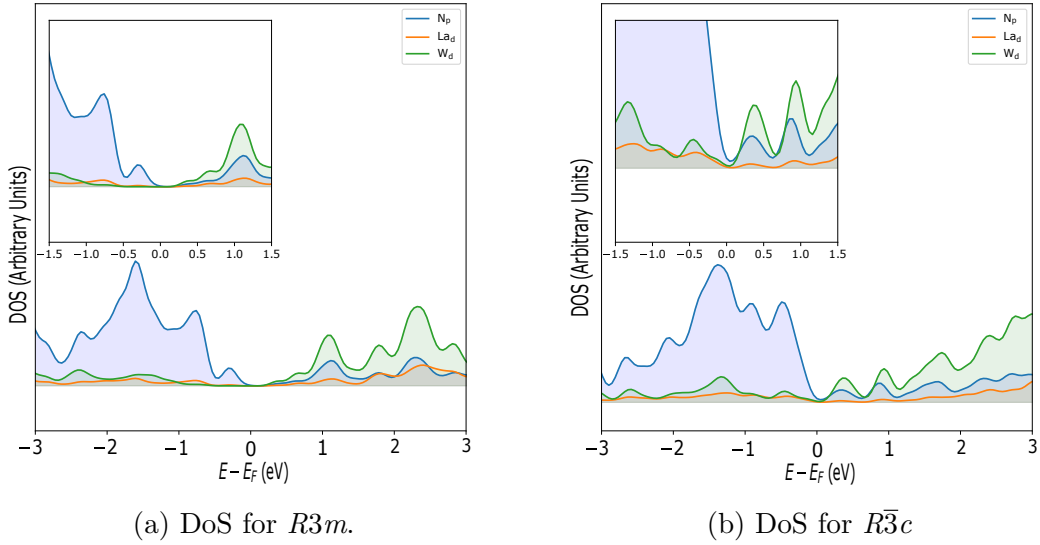
Figure 6.4: The DoS for bulk LaWN$_3$ in the $R3m$ and $R\overline{3}c$ space groups, as a function of the energy difference to the Fermi energy. The values below 0 shows the VBM, the band gap is the lack of states just above 0 and the CBM is where the states appear after 0.

6.1.6 Layer-resolved DoS

The layer-resolved DoS for the 71° DW is shown in Figure 6.5 with the five "unit cells" closest to the middle of the DW on each side, shown on the left and the resulting DoS on the right. The DoS is shown for the relevant orbitals for the VBM and the CBM, the N_p- ,La_d- and the W_d-orbitals [28]. The structure shows a reduction of the band gap, from around 0.8 eV in the middle of the domain to 0.5 eV at the DW, shown with the green and red vertical lines. The W_d -orbital is dominating the new states in the middle of the DW. The DoS shows a significant difference compered the middle of the domain at a distance of 7 Å from the middle of the DW and closer.
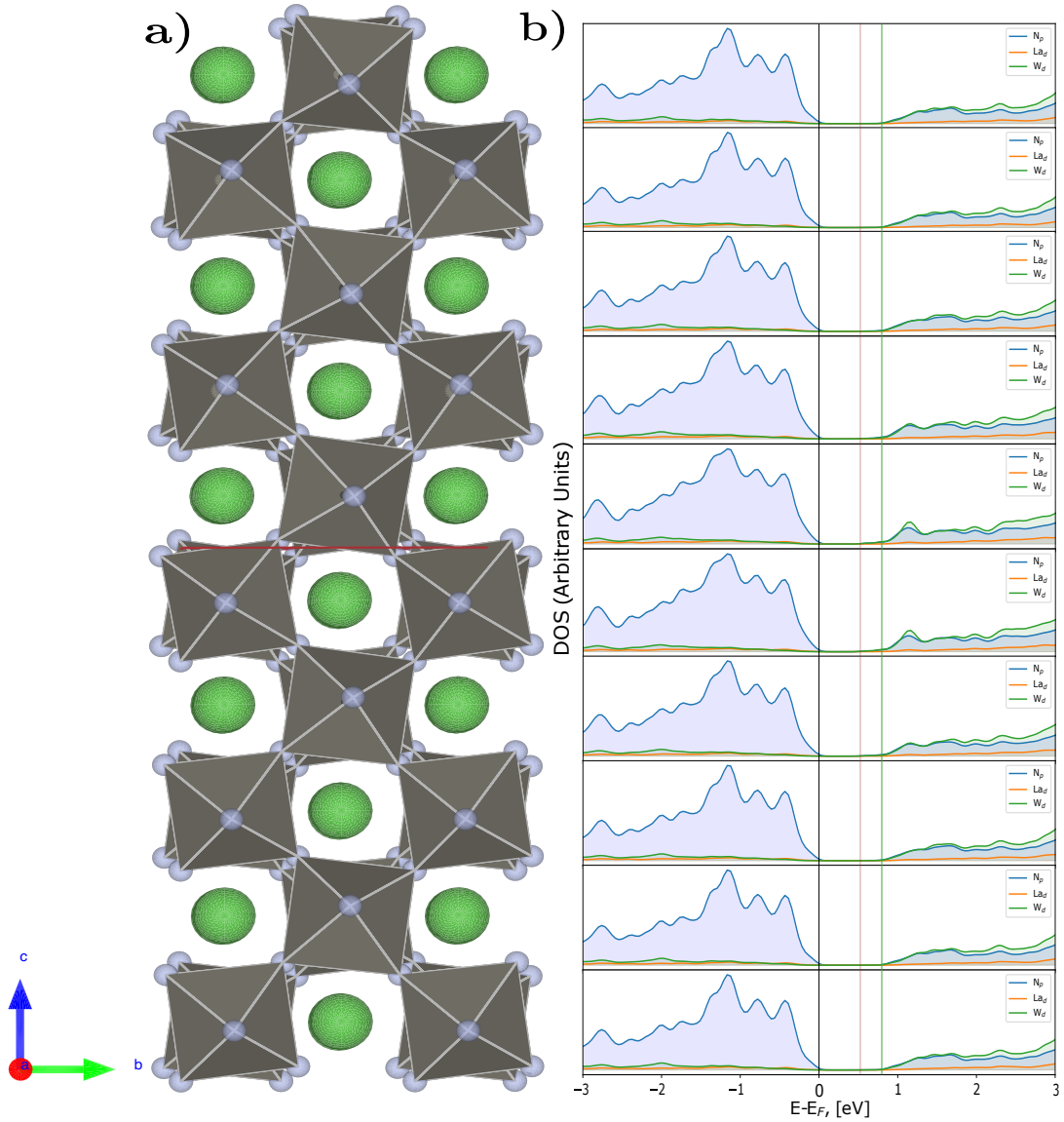
Figure 6.5: Layer-resolved DoS for 71° DW, b), with the corresponding unit cell shown in a). The middle of the DW is marked with a red plain in a). The bulk VBM and CBM is shown with the black and green vertical lines i b), respectively. The minimum CBM in the supercell is shown with the red vertical line in b).

For the 109° DW, the layer-resolved DoS shows states growing in the middle of the band gap from the center of the domain to the middle of the DW, see Figure 6.6. The contributions to the new states are first dominated by the nitrogen p-orbitals, but closer to the middle of the DW the d-orbitals of the tungsten atoms becomes the dominating contribution, with a peak centered 0.5 eV from the VBM. The layer-resolved DoS shows two peaks from the nitrogen p- and tungsten d-orbital which are not present in the middle of the domain, where the structure is closest to the bulk. A small number of states from the nitrogen p-orbital can be found in the middle of the band gap throughout the entire supercell. The 109° DW shows a significant reduction of band gap going from the middle of the domain, at 0.8 eV to the middle of the DW at around 0.3 eV, and a much larger change in the number of states in the middle of the DW than for 71° DW.
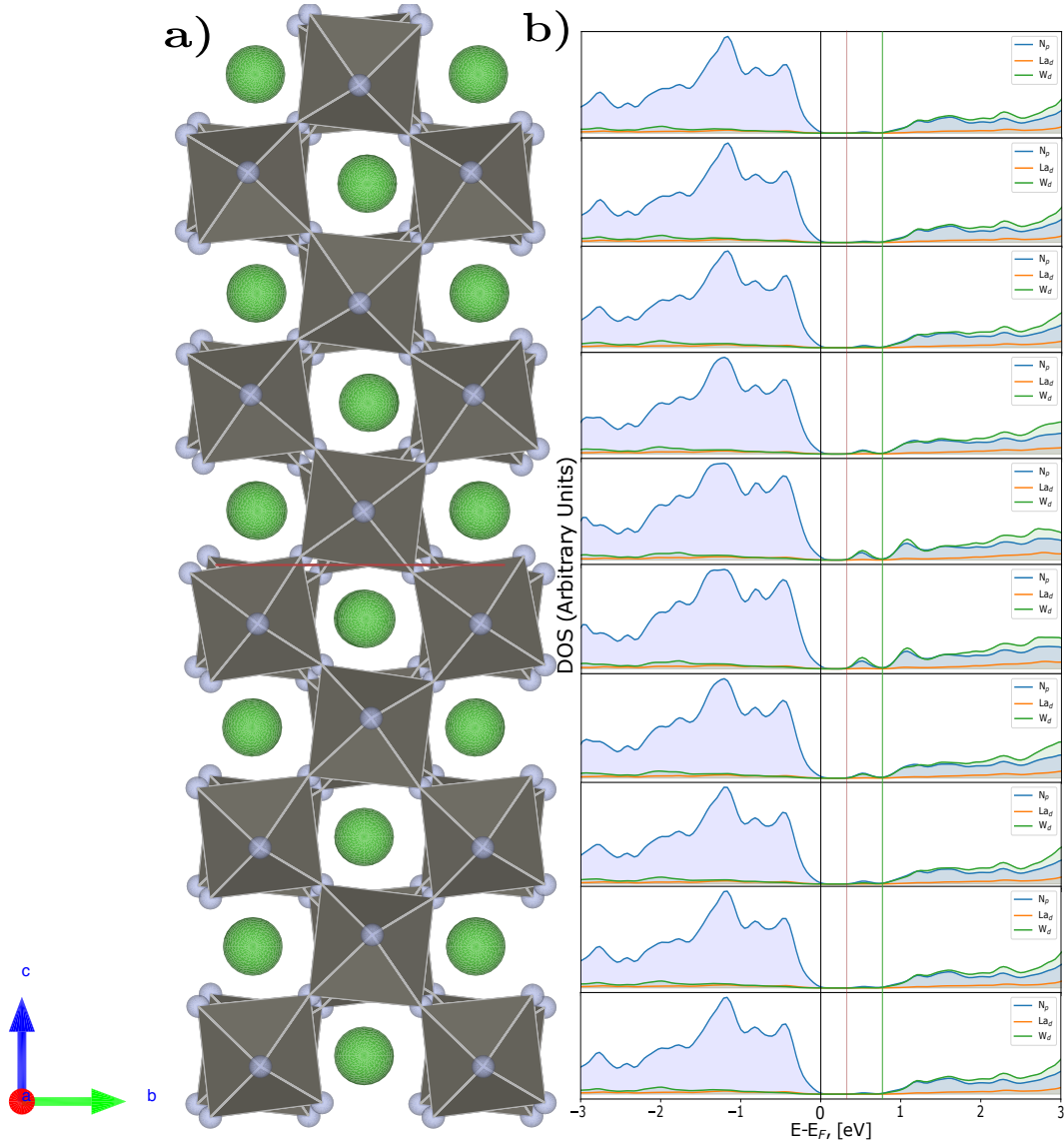
Figure 6.6: Layer-resolved DoS for 109° DW, b), with the corresponding unit cell shown in a). The middle of the DW is marked with a red plain in a). The bulk VBM and CBM is shown with the black and green vertical lines i b), respectively. The minimum CBM in the supercell is shown with the red vertical line in b).

The DoS of W_d- and N_p-orbitals grow in the middle of the band gap with two peaks for the 180° Y-DW as shown in Figure 6.7. The band gap disappears completely in the middle of the DW and is around 0.8 eV in the middle of the domain, with the new states being from the nitrogen p- and tungsten d-orbitals forming a peak in the middle of the band gap. Similar to the 109° DW, a small number of states from the nitrogen p-orbital is found in the middle of the band gap throughout the supercell.
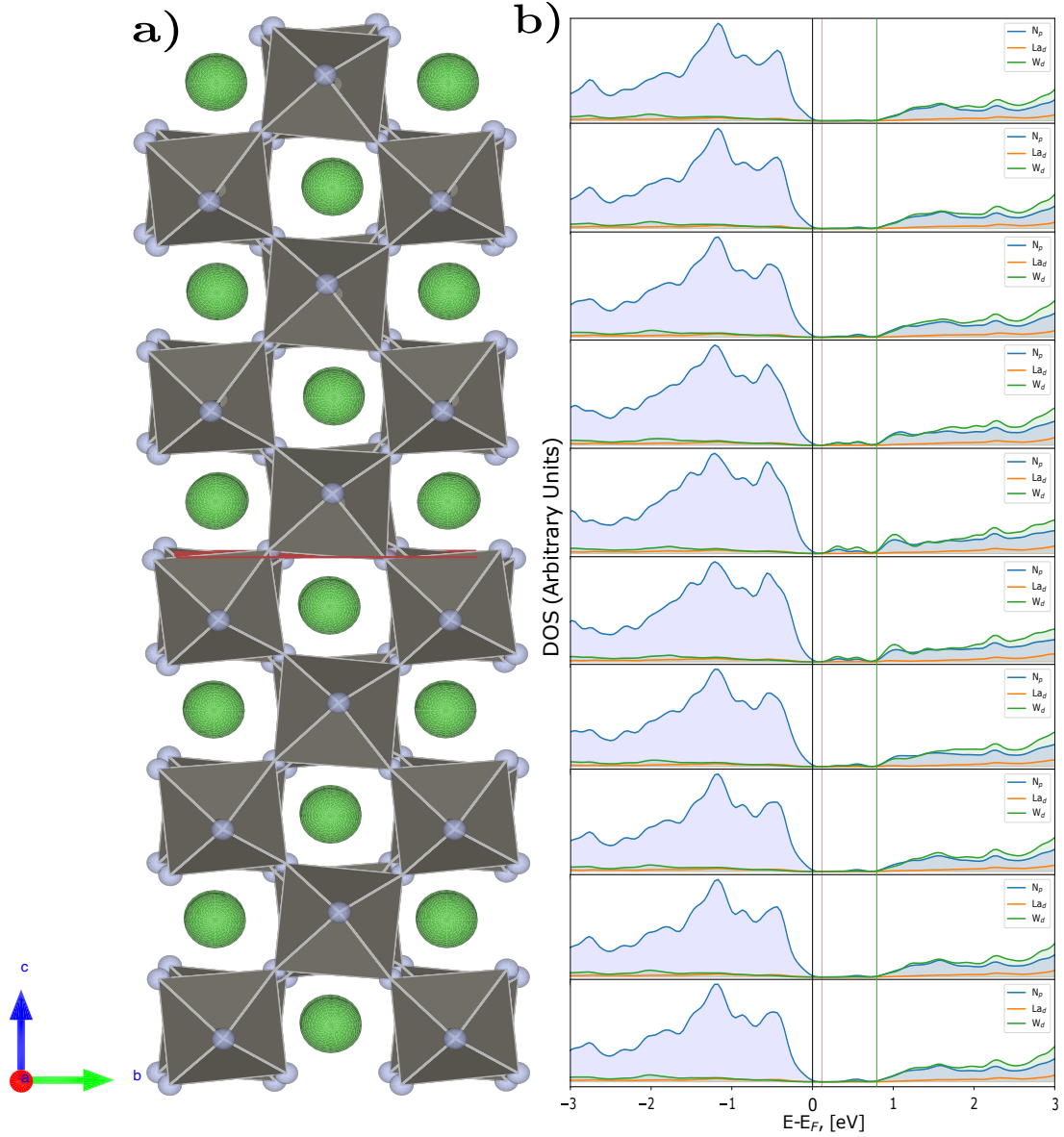
Figure 6.7: Layer-resolved DoS for 180° DW, b), with the corresponding unit cell shown in a). The middle of the DW is marked with a red plain in a). The bulk VBM and CBM is shown with the black and green vertical lines i b), respectively. The minimum CBM in the supercell is shown with the red vertical line in b).

6.2 Defects

6.2.1 Chemical Potential Diagram

The 2D chemical stability window for $LaWN_3$ is shown in Figure 6.8, with the chemical potential of lanthanum and tungsten shown as a function of the chemical potential of nitrogen. The diagram was constructed by using the formation energy of $LaWN_3$, LaN and WN_2 found in previous work [1]. From the formation energies, the chemical potential for the pure elements required for synthesis of $LaWN_3$ was found. A high value of the chemical potential, i.e. a value close to zero indicates rich conditions while a low value implies poor conditions of the element. The chemical potential range for nitrogen is much lower than for lanthanum and tungsten.
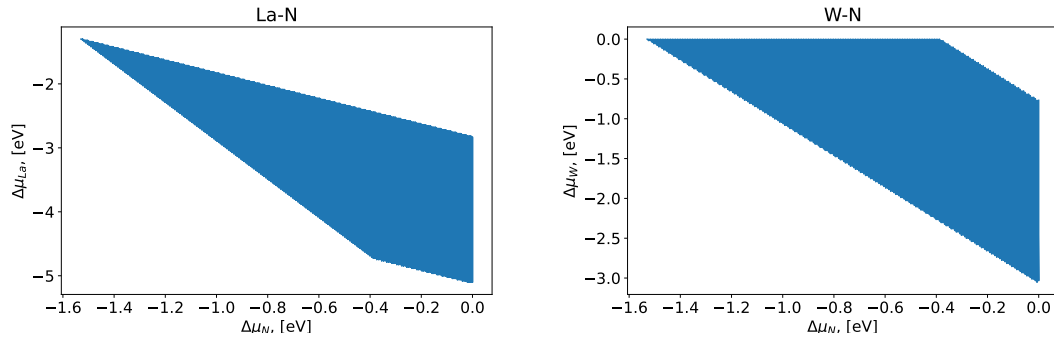
(a) Stability region for $LaWN_3$ for the chemical potential of lanthanum and nitrogen. (b) Stability region for $LaWN_3$ for the chemical potenital of tungsten and nitrogen.

Figure 6.8: 2D stability region in chemical potential space for $LaWN_3$.

The 3D chemical stability window for $LaWN_3$ is shown in Figure 6.9. The points A, B, C and D shows the extremal values for the chemical potentials where $LaWN_3$ is still favorable. These points are combinations of rich and poor conditions for the compositional elements. The extremal values are intersection points between different phases considered, LaN, WN_2, La, W, and N_2. The intersection points were used to construct the transition level diagrams with the chemical potential of the defects.
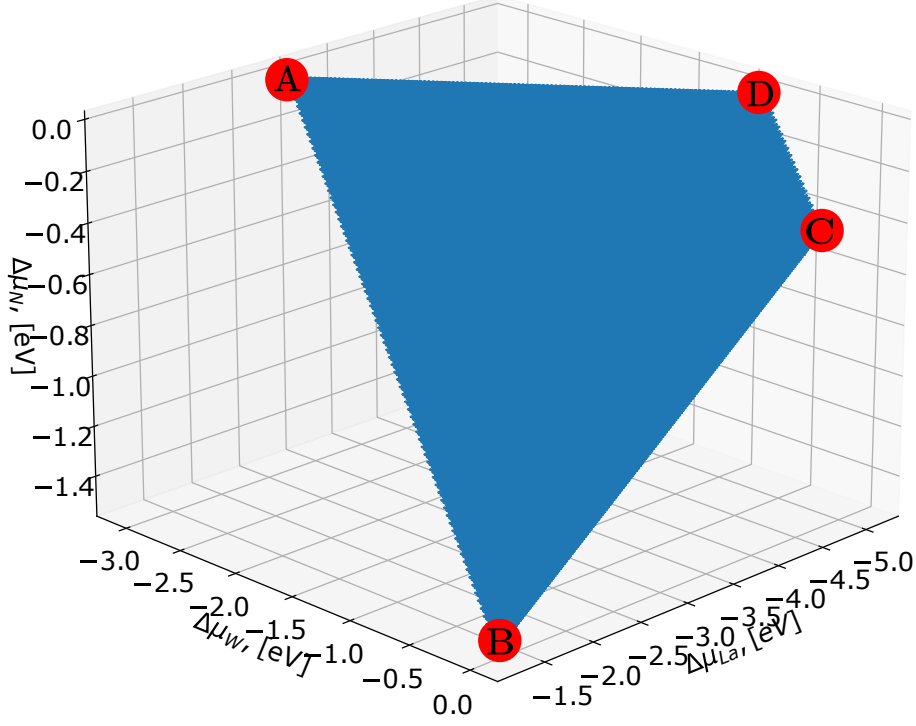
Figure 6.9: Chemical potential diagram of LaWN$_3$ with intersection points A, $\Delta\mu_{La}$=-2.8170 eV $\Delta\mu_W$=-3.7030 eV $\Delta\mu_N$=0 eV, B, $\Delta\mu_{La}$=-1.2805 eV $\Delta\mu_W$=0 eV $\Delta\mu_N$=-1.5365 eV, C, $\Delta\mu_{La}$=-3.5920 eV $\Delta\mu_W$=0 eV $\Delta\mu_N$=-0.7660 eV, D, $\Delta\mu_{La}$=-4.3580 eV $\Delta\mu_W$=-1.5320 eV $\Delta\mu_N$=0 eV.

6.2.2 Transition Level Diagrams

Transition level diagrams for the different points A($\Delta\mu_{La}$=-2.8170 eV, $\Delta\mu_W$=-3.7030 eV, $\Delta\mu_N$=0 eV), B($\Delta\mu_{La}$=-1.2805 eV, $\Delta\mu_W$=0 eV, $\Delta\mu_N$=-1.5365 eV), C($\Delta\mu_{La}$=-3.5920 eV, $\Delta\mu_W$=0 eV, $\Delta\mu_N$=-0.7660 eV) and D($\Delta\mu_{La}$=-4.3580 eV, $\Delta\mu_W$=-1.5320 eV, $\Delta\mu_N$=0 eV) in chemical potential space are shown in Figure 6.10. Nitrogen vacancy is the defect with the lowest formation energy for all conditions, with many conditions resulting in negative formation energy. There are no intersection points between the different defects in the band gap, suggesting that the Fermi level is located deep inside the conduction band. For the points A and B in the chemical potential space, where lanthanum is rich, the acceptor defect with the lowest formation energy is lanthanum antisite on the tungsten site. For the lanthanum poor conditions, points C and D, lanthanum vacancy is the acceptor defect with the lowest formation energy. For point A, the Fermi level lies just above the CBM, 0.28 eV above the CBM, while for point B, the Fermi level is 1.51 eV from the CBM, with lanthanum antisite on tungsten being the compensating defect for nitrogen vacancies. Nitrogen vacancy is compensated by lanthanum vacancies in the lanthanum poor conditions, point C and D. The Fermi level for point C is 0.77 eV higher than the CBM and for point D the Fermi level is 0.28 eV above the CBM.
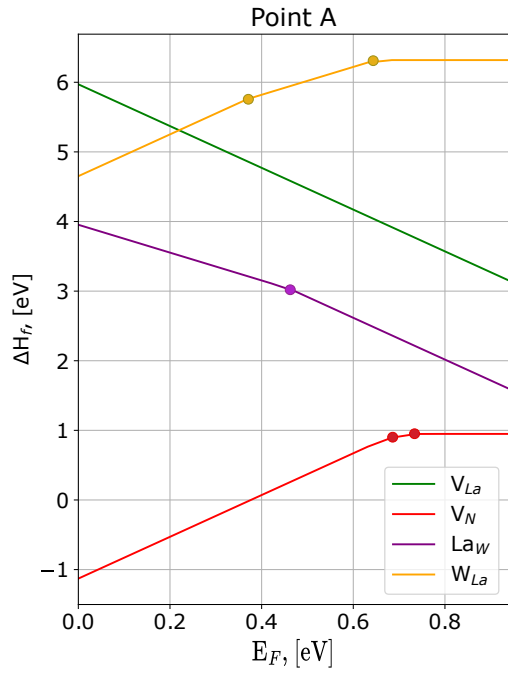
(a) Nitrogen rich/tungsten poor
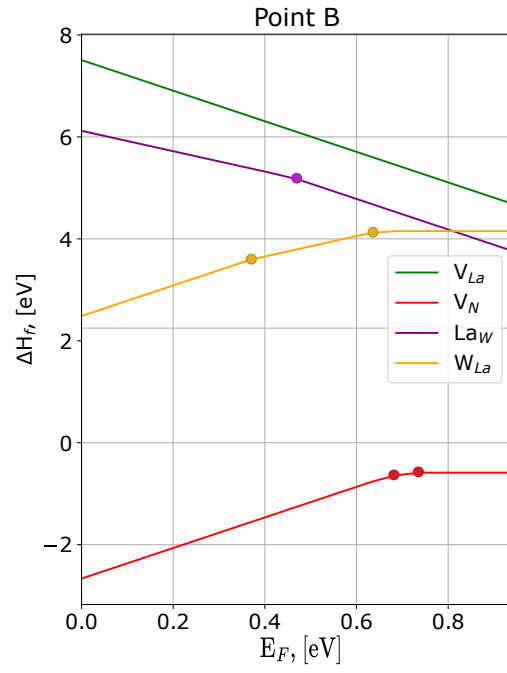
(b) Metal rich/nitrogen poor
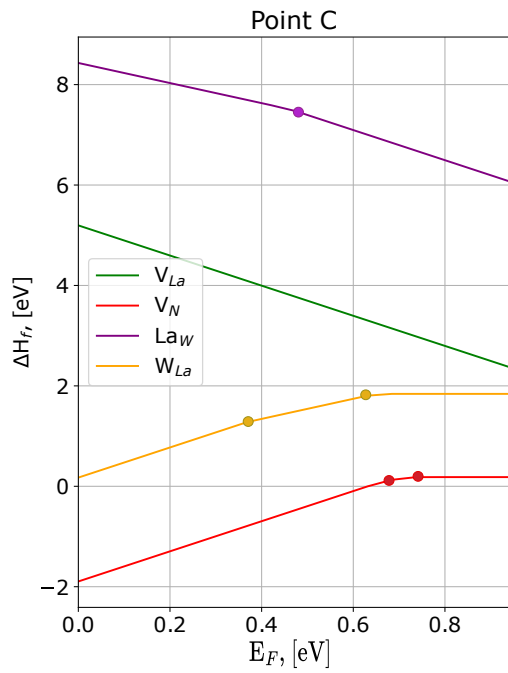
(c) Tungsten rich/lanthanum poor
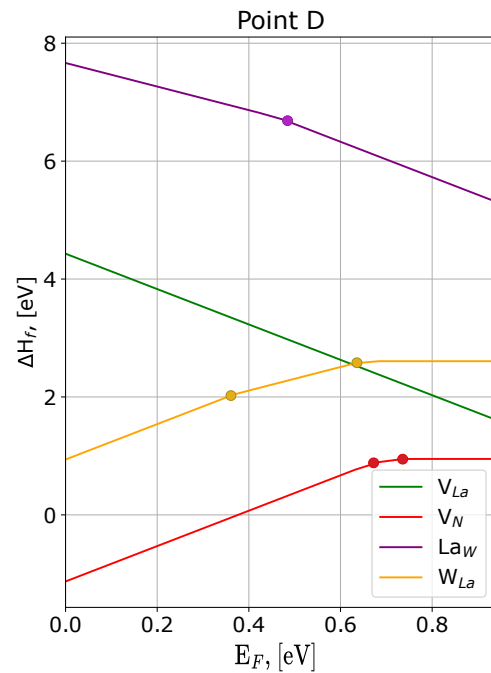
(d) Nitrogen rich/lanthanum poor

Figure 6.10: Transition level diagram for different points A, B, C, D in the stability window of LaWN$_3$. The transition level for the defects are marked with dots. The formation energy of the defect is given as a function of Fermi energy.

Oxygen substitution of nitrogen was included with nitrogen rich condition, point A($\Delta\mu_{La}$=-2.8170 eV, $\Delta\mu_W$=-3.7030 eV, $\Delta\mu_N$=0 eV) and nitrogen poor condition, point B($\Delta\mu_{La}$=-1.2805 eV, $\Delta\mu_W$=0 eV, $\Delta\mu_N$=-1.5365 eV). This was done for both oxygen rich condition with a p_{O_2} of 0.2 and oxygen poor condition, p_{O_2} of 10^{-8}, shown in Figure 6.11 .
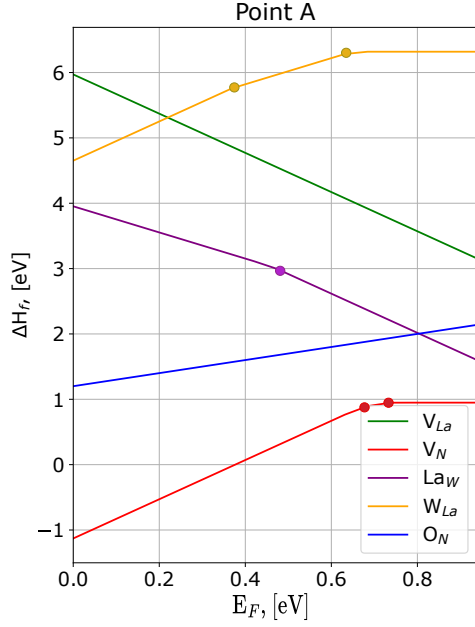
(a) Nitrogen and oxygen rich
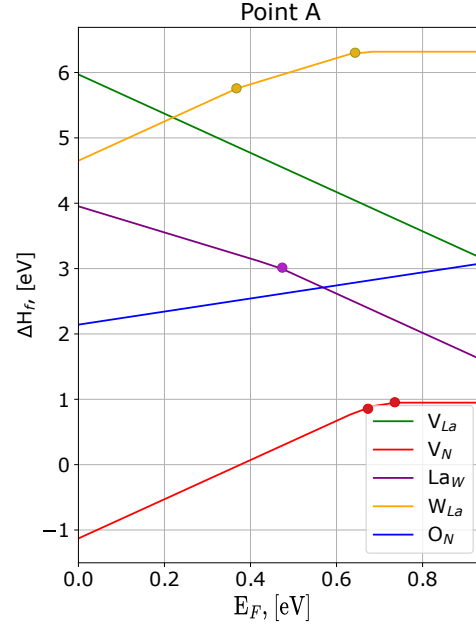
(b) Nitrogen rich/oxygen poor
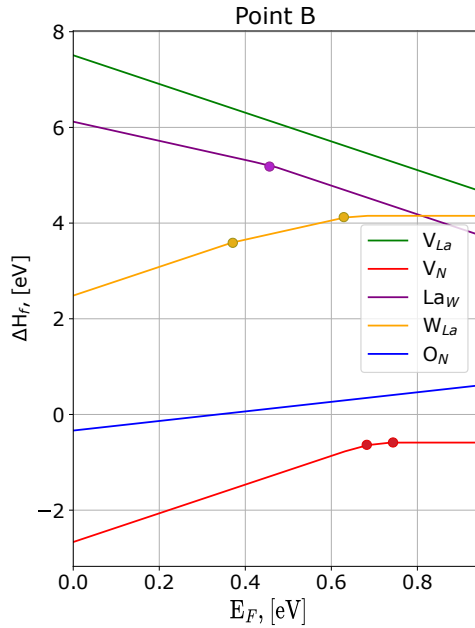
(c) Oxygen rich/nitrogen poor
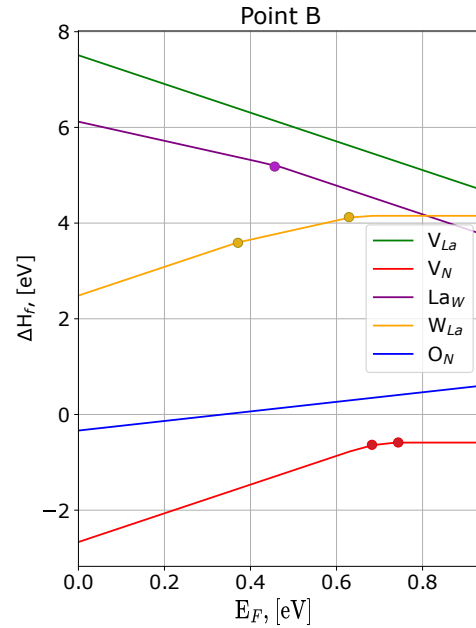
(d) Nitrogen and oxygen poor

Figure 6.11: Transition level diagram with oxygen present.

Oxygen substitution of nitrogen is a donor defect and has a higher formation energy than vacancy of nitrogen. This is valid for both nitrogen conditions (rich and poor) with both oxygen rich and oxygen poor conditions being considered. The formation energy of oxygen substitution of nitrogen having a charge of +1, is also lower than for the defect in a neutral cell for the entire band gap. Oxygen substitution of nitrogen has lower formation energy than the donor defect of antisite tungsten on lanthanum for low Fermi energies.

6.2.3 Transition Levels

The transition levels for the different defects are shown in Figure 6.12. Both the acceptor defects V_{La} and La_W have a transition level to a neutral state in the valence band. The transition for La_W, going from q=-3 to q=-2 lies in the middle of the band gap, thus being classified as a deep defect. Vacancy of nitrogen two transition levels in the band gap close to the CBM, being a shallow donor defect. Tungsten antisite on lanthanum also have two transition levels, but in the middle of the band gap being classified as deep defect states. Oxygen substitution of nitrogen is a donor defect with a transition level 0.1 eV above the CBM.
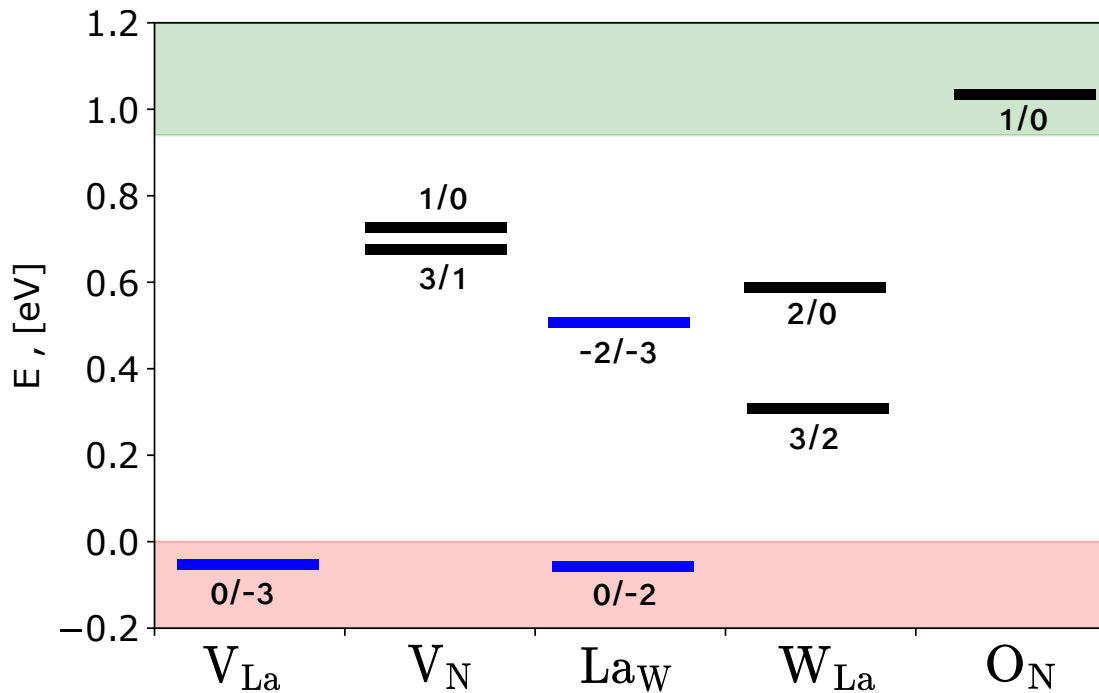
Figure 6.12: Transition levels for different defects, donor defects shown in black and acceptor defects in blue. Red area is the VBM, green is the CBM and white is the band gap.

6.2.4 Migration Barrier

The migration barrier for $V_N^\times$ and $V_N^{\bullet\bullet}$ is shown in Figure 6.13 as a function of migration distance. The migration barrier for $V_N^\times$ is 0.698 eV, and for $V_N^{\bullet\bullet}$ the migration barrier is 0.679 eV. The migration path for the nitrogen vacancy is 3.44 Å between the nitrogen sites on the tungsten atom.
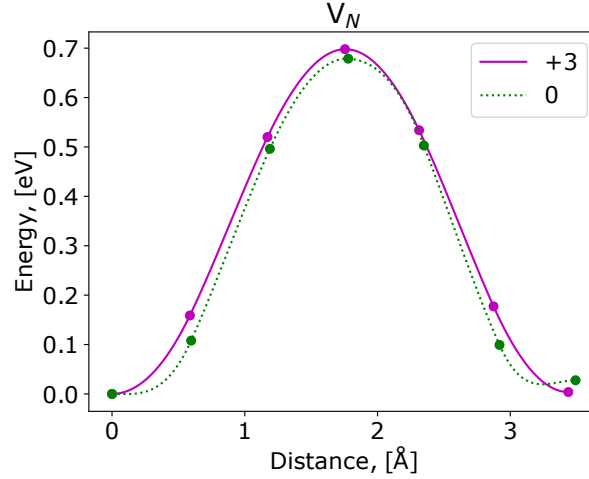
Figure 6.13: Energy barrier for migration for a nitrogen vacancy with different charge. The distance shown is the migration distance to the nearest site for the vacancy. The label gives the charge of the defect cell. Dots marks the energy of the images and lines is the interpolated curves.

The migration barrier for $V_{La}^\times$ and $V_{La}^{'''}$ is shown in Figure 6.14 as a function of the migration path. The migration barrier for $V_{La}^{'''}$ is 4.584 eV and for $V_{La}^\times$ the migration barrier is 4.482 eV. The migration path for V_{La} is 5.10 Å, between the neighbouring lanthanum sites in the structure.
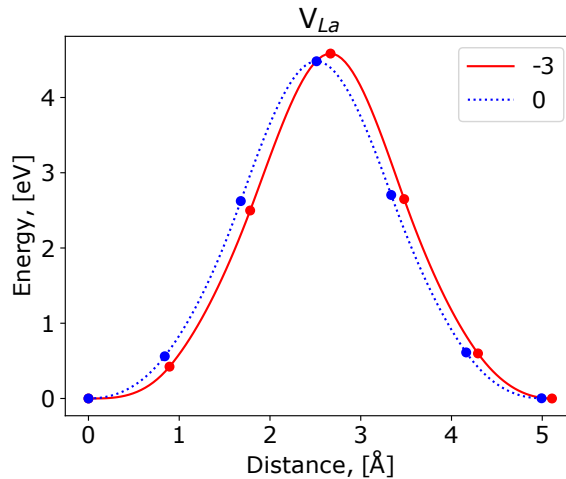
Figure 6.14: Energy barrier for migration for a lanthanum vacancy with different charge. The distance shown is the migration distance to the nearest site for the vacancy. The label gives the charge of the defect cell. Dots marks the energy of the images and lines is the interpolated curves.

7 Discussion

7.1 Domain Walls

7.1.1 Formation Energy and Structural Parameter

Rhombohedral perovskites have, in principle, four types of parallel DWs; 180° X-, 180° Y-, 109° and 71° DWs. In LaWN$_3$, the primitive unit cell angle is close to 60 degrees, resulting in small distortions from ground state structure to pseudocubic structure, hence the ferroelastic transition of the unit cell costs little energy. The 71° DW has the lowest formation energy of the DWs, almost one third of the formation energy of the other DWs, indicating that 71° DW is the dominant DW in LaWN$_3$. The energy difference of almost 10 meV/Å^2 above the formation energy of the 71° DW predicts the other DWs to be less likely to form. In the 71° DW, the distortions in the W-N bond length are much smaller than for the other DW types. In contrast, the bond angles in the 71° DW deviate more from the bulk values than in the 180° Y-DW. These findings show that the bond length distortions cost much more energy than the bond angle distortions. For the 109° DW, bond length distortions are comparable with the 180° Y-DW, but have larger bond angle distortions, resulting in the highest energy of the DW. The polarization change is sharpest across the DW for the 71° supercell, showing effect of the small displacement of the tungsten atom from the bulk position throughout the supercell compared to 109° and the 180° Y-DW, where the polarization changes more gradually.

The present study is focused on the Y-DW, but from the formation energy and the bond lengths for the 180° X-DW suggest similarities with the 180° Y-DW. The bond length distortions are greatest for the X-DW, meaning that the tungsten atom is placed almost in the center of the nitrogen octahedra in the middle of the DW. Since both the X- and Y-180° DW have similar formation energies, the X-DW should have less deviation in the bond angles across the supercell like what was observed in the 180° Y-DW.

For the well-studied perovskite BiFeO$_3$, the 109° DW has the lowest formation energy and the 71° DW has the highest formation energy, in sharp contrast to the DWs in LaWN$_3$. This effect was attributed to oxygen octahedra mismatch across the DW in BiFeO$_3$ [74]. Octahedral mismatch will result in a large deviation from bulk values in the in-plane and out-of-plane bond angles in the octahedra. Lubk et. al [75] found that the 109° DW in BiFeO$_3$ has a formation energy of 12.80 meV/Å^2, while the 71° DW had a formation energy of 22.66 meV/Å^2. The difference between the lowest and highest formation energy in BiFeO$_3$ is similar to the corresponding values in LaWN$_3$, but the formation energy of the specific DWs in LaWN$_3$ is much lower. The lowest formation energy of DW in PbTiO$_3$ and LiNiO$_3$ is 7.83 meV/Å^2 [76] and 9.99 meV/Å^2 [55], respectively. For both these perovskites, the lowest formation energy DWs are the 180° DWs. The formation energy of the 71° DW in LaWN$_3$ is 5.01 meV/Å^2 which is a considerably lower formation energy value of the DW than the DWs in typical ferroelectric oxide perovskites. On the other hand, a very low formation energy of 0.50 meV/Å^2 was found for the 180° DW in the hybrid halide

perovskite MAPbI$_3$, where MA is methylammonium [77]. Based on the limited set of comparisons regarding the lowest formation energy DW, LaWN$_3$ has a significantly lower formation energy of the DW compared to the oxide perovskites, but much higher than the example of a halide perovskite above.

7.1.2 DW Width, T$_c$ and Domain Size

The DW width can be estimated from the structural parameters like bond angle, polarization and bond lengths. The DW width is 14 Å for the different DWs in LaWN$_3$. The DW width for PbTiO$_3$ is 5Å [78] and BiFeO$_3$ have a DW width of 12 Å found from the data provided by Lubk et. al [75]. The wider DW in LaWN$_3$ compared to oxide perovskites can be attributed to the smaller ferroelastic deformation of the unit cell and the low energy cost of distorting the W-N-W bond angle, resulting in a larger volume of distorted structure. A large DW width can indicate a low transition temperature, T$_c$, because the distortions in the structure does not cost much energy and is therefore favorable for the DW to spread over a larger volume. If the distortion does not cost a lot of energy, the structure will quickly change upon heating. The half-width of the DW, w, is

$$w = \frac{\sqrt{2}c_0}{\sqrt{A \mid T - T_c \mid}}, \tag{28}$$

where A is the second order coefficient for the Landau-Ginzburg expression of the Gibbs free energy and c_0 defines some characteristic velocity [79]. A wide DW hence results in a low T_c, with DFT calculations being 0 K calculations. Abrahams et. al [80] found an empirical correlation between the polarization and T$_c$ in ferroelectrics, however most of their work was on ferroelectric oxides. By using the displacement of the tungsten atom found for the optimized $R3c$ structure of LaWN$_3$, the Curie temperature can be estimated to 1100 K. However, there is significant scatter in the data from Abrahams et. al and the Curie temperature should only be taken as a first estimate.

The low energy cost of forming the 71° DW in LaWN$_3$ compared to the lowest formation energy DW in perovskite oxides indicate many small domains will form upon transition to the ferroelectric phase. However, this effect is not *a priori* given because electrostatic interactions between domains with different polarization has an implicit energy cost. The mobility of the DW could also result in much larger domains than what the formation energy of the DW should indicate, as small domains can merge into large domains. Defects in the structure can also interact with the DWs. Hence, by pinning the DW and promoting different types of DW, the size of the domains is not only a result of the formation energy of the DW, but also other factors also come into play.

7.1.3 DoS for DW

The layer-resolved DoS shows a significant reduction in the band gap for all the DW types in LaWN$_3$ compared to the bulk values. The reduction in the band gap is explained by the second order Jahn-Teller effect. The tungsten atom in the bulk state is moved towards the centrosymmetric position in the nitrogen octahedra found in the DW. This movement introduces less overlap between the nitrogen p- and tungsten d-orbital thereby lowering the energy of the empty orbitals which closes the band gap, see Figure 2.1. The least displacement of the tungsten atom from the bulk state to the middle of the DW compared to the other DW types is found in the 71° DW, as seen in the polarization plot, Figure 6.3. This explains why the 71° DW showed the smallest reduction of the band gap of the considered DW types. For the 180° DW, which had the largest displacement of the tungsten atom towards the centrosymmetrial position in the middle of the DW, naturally showed the greatest reduction in band gap, resulting in a metallic DoS in the middle of the DW.

The bulk DoS calculations of the $R3m$ and $R\bar{3}c$ space groups of LaWN$_3$ showed that the non-polar $R\bar{3}c$ have no band gap, while the untilting of the octahedra in the $R3m$ resulted in a small reduction in the band gap compared to the ground state $R3c$ structure. The DoS for the bulk $R3m$ is nearly identical to the layer-resolved DoS for 71° DW in the middle of the DW, meaning that the local structure in the middle of the 71° DW resembles the $R3m$ structure. This similarly can be observed in the bond angles, where the in-plane angle of the 71° DW is almost 180 degrees in the middle of the DW, indicating that the octahedra are almost not tilted. For the 109° and the 180° DW, the layer-resolved DoS resembles the DoS for $R\bar{3}c$, with two sharp peaks dominating the CBM, hence suggesting that the local structure in the domain walls resembles the non-polar $R\bar{3}c$ structure. This resemblance agrees with the polarization, bond length and the bond angles in the DWs. The polarization and bond length shows a large displacement of the tungsten atom towards the center of the nitrogen octahedra, thus lowering the polarization and moving the short and long bond lengths closer to each other. The in-plane angles show a reduction in tilting of the octahedra in the middle of the DW, especially for the 109°. This results show that the displacement of tungsten is the dominant effect for the DoS in the DW compared to tilting of octahedra in the structure.

The DoS calculations in this project were performed with the PBEsol functional. A limitation of this functional is an underestimation of the band gap in the structure, giving a value of 0.94 eV found in this project compared to 1.72 eV found with the more accurate hybrid functional used by Fang et. al [30]. The large reduction of the band gap in the DW compared to bulk could therefore be interpreted as an artifact of the functional used. However, the calculations in the previous work [1], showed a total closure of the band gap for the non-polar rhombohedral structures, $R\bar{3}c$ and $R\bar{3}m$ using the hybrid functional HSE06. This result shows the large effect the non-polar transition will have on the band gap in LaWN$_3$. While a metallic DoS might not actually be fully realized in the 180° DW, a large change in the band gap is still expected in the middle of the DW compared to the bulk value.

Band gap closing in the DW has also been observed in other perovskites. Seidel et.

al [78] also found a reduction in the band gap for 71°, 109° and 180° DW in $BiFeO_3$, similar to the result above. Similarly to $LaWN_3$, the 109° and 180° DW in $BiFeO_3$ had the greatest reduction in band gap, however, the effect was more modest. The 109° DW had a reduction of about 0.1 eV while the 180° DW had a reduction of 0.2 eV compared to band gap of bulk $BiFeO_3$. In $LiNbO_3$, the band gap was reduced by 12% in the DW compared to bulk for the 180° Y-DW [81]. This is a much lower reduction in the band gap compared to $LaWN_3$, where the band gap was reduced by 47% for the 71° DW, 68% for the 109° DW and no band gap for the 180° DW. A lowering of the band gap was also found for hybrid perovskite halides by Liu et. al [77]. They found that the band gap could be reduced by 20-40% from bulk values to charged 180° DW for different hybrid lead halide perovskites. The reduction in band gap could be as large as 0.5 eV for $MAPbCl_3$, with a band gap going from 2.39 eV in bulk to 1.89 eV in the 180° charged DW. $LaWN_3$ shows a larger reduction in the band gap than the considered oxide and hybrid halide perovskites, with even a total disappearance of the band gap in the 180° DW. The large difference between the band gap in bulk and the parallel DW found in $LaWN_3$ seems quite unique, where the bulk state in $LaWN_3$ is semiconducting, while the 180° DW shows metallic DoS. For most perovskites with conducting DW, the material is insulating in bulk, and charged DW increases the conductivity in the DW, due to the accumulation of charge carriers in the DW [82].

7.1.4   Conducting DW in $LaWN_3$

The significant change in the DoS for the DWs in $LaWN_3$, especially for the 180° DW, supports the potential use of $LaWN_3$ in ferroelectric logical and memory devices using conducting DWs. The DWs in $LaWN_3$ showed a much larger reduction in the band gap from the bulk state compared to $BiFeO_3$. $BiFeO_3$ was used by Sharma et. al as a material for a potential ferroelectric memory device [9]. The device showed only small currents from the DWs, limiting the practical utility of the device. The larger difference in the band structure in $LaWN_3$ suggest that the conductivity in the DWs could be greater than that for $BiFeO_3$ DWs. A higher conductivity in the DW means that less power is needed for the FeRAM function, and therefore a $LaWN_3$ based device is expected to be more efficient and sustainable.

Conducting DW has been observed in thin film $BiFeO_3$, for both 71° and 109° DWs [83]. The conductivity in the DW was explained by oxygen vacancies accumulating at the DWs, creating n-type carriers and intermediate states in the band gap. Rojac et. al [84] observed p-type conductivity in 109° DW attributing the effect to bismuth and iron vacancies in the structure, accumulating in the DW. Together with the reduction in band gap in the DW from the transition towards a non-polar state, the defects introduce charge carriers in the DW, thus increasing the conductivity compared to bulk. $LaWN_3$ has a much larger reduction in the band gap, increasing the number of charge carriers in the DW compared to bulk through Eq. 3 and 4. The increased number of charge carriers will increase the conductivity of the material as explained in Eq. 2. However, the reduction in the band gap does not influence the mobility of the charge carriers and does therefore not guarantee DWs with a significantly better conductivity.

The minimum effective mass for electrons in bulk $R3c$ LaWN$_3$ was found to be 0.523, and 0.267 for the $R3m$ space group [1]. Because of the lower effective mass, higher mobility of the charge carriers in the $R3m$ space group is expected. The mobility of the electrons thus changes with the different space groups. As the local structure in the 71° DW approaches the $R3m$ structure in the middle of the DW, the mobility of the charge carriers also increases from the bulk $R3c$ structure, resulting in an expected higher conductivity in the 71° DW than the bulk structure. However, as all calculations on the mobility was made on the bulk material, the results only indicating the effective mass of charge carriers in the DWs.

7.2 Defects

7.2.1 Stability Window and Formation Energy

As seen in the chemical potential diagram, Figure 6.9, the synthesis of LaWN$_3$ requires nitrogen-rich conditions, the chemical potential of nitrogen varies from 0 to -1.54 eV. Synthesis of LaWN$_3$ is therefore often performed under ultra-high vacuum and at temperatures ranging from 973 to 1573 K, in order to achieve the required nitrogen-rich conditions [32][85]. The chemical potential diagram also shows that the chemical potential for lanthanum cannot be too high without forming the competing phase LaN or pure La. This agrees with the study by Hanzawa and Hiramatsu [39], where they found that with a lower power of the sputtering of tungsten compared to lanthanum, LaN formed together with LaWN$_3$. The stability window found for LaWN$_3$ also resembles what was found by Geng and Xiao with some discrepancies in the chemical potential for lanthanum [34].

The formation energy of oxygen substitution of nitrogen is higher than the formation energy for nitrogen vacancies, both under nitrogen rich and poor conditions combined with rich and poor conditions of oxygen, suggesting that the LaWN$_3$ is more likely to take a chemical composition of LaWN$_{3-\delta}$ rather than LaWN$_{3-\delta}$O$_\delta$. The formation energies for the defects found in the present work are slightly lower than the energies found by Geng and Xiao [34], with a negative formation energy for $V_N^\times$ in nitrogen poor conditions. A negative formation energy does not mean that LaWN$_3$ is unstable, because the calculations are done in the dilute limit, with no regards to kinetic effects. The low formation energy for nitrogen vacancies, also agrees with synthesis studies showing the difficulty to form LaWN$_3$ with a stoichiometric ratio of 1:1:3 [37][38].

7.2.2 Migration Barrier

The small difference in the migration barrier between the differently charged vacancies for both nitrogen, $V_N^\times$ and $V_N^{\bullet\bullet\bullet}$, and lanthanum, $V_{La}^\times$ and $V_{La}^{'''}$ respectively, shows that the migration barrier is not dependent on the charge of the defect cell. The migration barrier for nitrogen vacancy is similar to that of oxygen in commonly used perovskite oxides like BaTiO$_3$ (0.67 eV), SrTiO$_3$ (0.46 eV) and LaAlO$_3$ (0.64 eV) [86]. The low migration barrier for nitrogen vacancy was not expected, as the

nitrogen atoms are regarded as more covalently bonded, which is stronger bonded, compared to the more ionic bonding in the oxide perovskites. The ionic radius for 6-fold coordinated oxygen with charge -2 is similar to the 6-fold coordinated nitrogen with charge -3 [87]. The migration barrier for the nitrogen vacancy in $LaWN_3$ is much lower than the migration barrier for nitrides like BN, with graphite structure, and hexagonal GaN, with wurtzite structure, where the migration barrier is 5.8 and 2.6 eV, respectively [88][89]. The difference in migration barrier for nitrogen vacancy in $LaWN_3$ and other nitrides is probably due to the difference in the covalency of the bonds in the materials. Where the nitrogen atoms in $LaWN_3$ have a mixed ionic-covalent bond to tungsten, the nitrogen atoms have strong covalent bonds to boron and gallium. The B-N bond length is hence much shorter, 1.45 Å [90], compared to the bond length in $LaWN_3$ showing that the bonding is much stronger in BN, resulting in a high migration barrier for vacancies in the structure. The difference in crystal structure between $LaWN_3$ and the other nitrides can also explain why the migration barrier is much lower in $LaWN_3$, where the vacancy can jump between equivalent sites on the octahedron.

The migration barrier of lanthanum vacancies in $LaWN_3$ is also similar to perovskite oxides with the migration barrier in $LaMnO_3$ being 3.93 eV in the cubic phase [91]. The migration barrier for lanthanum vacancy in $LaWN_3$ is high, and the defect is thus not mobile, especially compared to nitrogen vacancies. The much longer diffusion path for the V_{La}, 5.1 Å, compared to V_N, 3.44 Å, can explain the larger migration barrier for lanthanum vacancy in $LaWN_3$.

Low mobility of defects in a material often indicates good refractory stability. $LaWN_3$ is expected to have better refractory stability than oxide perovskites due to the more covalent bonding in the material compared to the ionic bonding found oxide perovskites. The migration barrier for V_{La} in $LaWN_3$ is large, 0.55 eV larger than in $LaMnO_3$, while the migration barrier for V_N is surprisingly low, comparable to V_O in oxide perovskites. This finding could suggest that $LaWN_3$ may not have the excellent refractory stability expected for a nitride perovskite compared to oxide perovskites.

7.2.3   Transition Levels and Charge Carriers

As outlined above, nitrogen vacancy is the dominating defect in $LaWN_3$ having the lowest formation energy of the defects considered. However, vacancies of nitrogen need to be compensated, either by other defects or by electrons. For the lanthanum poor conditions, points C and D, the compensating defect is V_{La}''' and for the lanthanum rich conditions, points A and B, the compensating defect is La_W''', both types of defects give Fermi level well inside the conduction band. Because of the high Fermi level of the compensating defects, free electrons are likely to contribute to compensation for vacancy of nitrogen, especially for low defect concentrations. The formation energy for nitrogen vacancies are low, suggesting a large number of defects are often present in the material, consequently resulting in a large amount of charge carriers in the structure.

The transition level of $V_N^\bullet$ to $V_N^\times$ gives a trap state 0.22 eV below the CBM. This trap state is close to the CBM, being a shallow defect, giving a $k_b T$ value of 2500 K to thermally excite the electron to the conduction band. While this is much higher than the estimated Curie temperature for LaWN$_3$, charge carriers from the trap state is expected to be exited to the conduction band due to to the Fermi-Dirac distribution of the electrons at temperatures higher than 0 K, in consort with other promotion methods like photons or electric fields. Charge carriers in the deep trap states, far from the band edges, are not mobile as they need a lot of energy to be promoted. Defects in BiFeO$_3$ were studied by Geneste et. al [92]. The conductivity of the DW in BiFeO$_3$ was explained by vacancies in the structure accumulating at the DW. The transition level for oxygen vacancies was in the middle of the band gap, while the transition level for iron and bismuth vacancies was closer to the VBM, 0.53 eV and 0.16 eV, respectively. The transition level for bismuth is close in energy to the nitrogen vacancies in LaWN$_3$, but with a formation energy much larger than for nitrogen vacancies, 2 eV for V_{Bi} in oxygen-rich conditions versus 1 eV for V_N in nitrogen-rich conditions. This suggest that a larger amount of charge carriers from defects are present in LaWN$_3$ compared to BiFeO$_3$, with a similar trap state energy, increasing the conductivity. This shows the potential for conductance of charge carriers from defects in LaWN$_3$.

The low energy barrier for migration of nitrogen vacancies, suggest that the vacancies can accumulate in the DW, where they are more stable because of the deformation of the structure in the DW, providing favourable sites for the defects. The nitrogen vacancies are compensated by electrons or acceptor defects. As the CBM is significantly lower in the DW than the bulk structure, compensating electrons can be thermally excited to the conduction band. The small band gap in the 109° DW and no band gap in the 180° DW suggest that very little or no thermal energy is needed to promote the compensating electrons to the conduction band, increasing the amount of free charge carriers drastically in the DWs. However, the calculations done on the transition levels are for bulk material but can indicate how defects behave in the DW.

8 Conclusion

The first aim of this project was to investigate the possible presence of conducting DW in $LaWN_3$ through DFT calculations. The ferroelastic 71° and 109° DW were simulated together with the 180° X- and Y-DW. The 71° DW was found to have the lowest formation energy, a finding attributed to the small ferroelastic distortion needed for the primitive unit cell and to the small distortion of the W-N bond length in the DW compared to the 109° and 180° DWs. In $LaWN_3$, the distortion of the W-N bond lengths in the structure cost more energy than the distortion of the W-N-W bond angles.

The layer-resolved DoS analysis of the different Y-DW showed a significant decrease in the band gap in the middle of the DW compared to the bulk state in the middle of the domains for all the DW types. This reduction in the band gap was attributed to the second order Jahn-Teller effect, with a small displacement of the tungsten atom in the nitrogen octahedra compared to bulk. The local structure in the DW was found by comparing the DoS with bulk DoS calculations for different space groups. The 71° DW resembled the $R3m$ configuration while the 109° and 180° DW were similar to the $R\bar{3}c$ structure. The 180° DW had the largest reduction in the band gap, showing a metallic DoS in the middle of the domain wall. The reduction in the band gap in the DWs in $LaWN_3$ are larger than what has been reported for both oxide and halide perovskites.

The second aim of this project was to investigate the defect chemistry of $LaWN_3$ in order to get a better understanding of the material and defects in nitrides in general. This aspect was also undertaken through DFT calculations. The stability window for $LaWN_3$ showed that nitrogen-rich conditions are needed to synthesis the compound, agreeing with experimental synthesis studies performed on the material. Nitrogen vacancies had the lowest formation energy of the intrinsic defects and were lower than oxygen substitution with nitrogen, indicating that nitrogen vacancy is the dominating defect in the structure. NEB calculation on the vacancies in the structure revealed that the mobility of nitrogen vacancies is similar to oxygen vacancies in oxide perovskites, while the migration barrier for lanthanum vacancies was very high, as expected, and similar to that of La-containing oxide perovskites.

The conclusion that can be drawn from this project is that $LaWN_3$ shows great potential for use in FeRAM applications with conducting DWs as the basis of working principle. The layer-resolved DoS indicates that $LaWN_3$ will have a significant increase in the conductivity from the bulk state towards the DW with more charge carriers in the DW. The reduction in the band gap in the DW was much larger than what is observed in materials used for current state-of-the-art FeRAM devices with conduction DWs. The migration barrier for nitrogen vacancies was surprisingly low, indicating that $LaWN_3$ does not have the anticipated higher thermal stability, than typical oxide perovskites.

9 Further work

In this project, the electronic structure of the different DWs in LaWN$_3$ was evaluated by the layer-resolved DoS. Using this approach one can indicate the amount of charge carriers in the DW, but the DoS does not include the mobility of the charge carriers. The mobility of the charge carriers in the structure can be found through band structure analysis. A band unfolding of the DW should be performed to evaluate the mobility of the charge carriers and thereby getting a better estimate of the conductivity of the different types of DWs in LaWN$_3$.

To obtain a better understanding of the domain structure of LaWN$_3$, a NEB study of the mobility of various DWs should be done. The mobility of the DW, especially for the dominating 71° DW, must be addressed to get an estimate of the domain size in the structure. The focus of this study was on the Y-DWs in LaWN$_3$. The properties of the 180° X-DW remain unknown and should be investigated further.

The defect calculations in this project were performed on bulk LaWN$_3$. As the calculated migration barrier for nitrogen vacancies was surprisingly low, similar to oxygen vacancies in oxide perovskites, the defects are mobile and could accumulate in the DW. The interaction between the defects and the DW is therefore important, as the defect can pin the DW or promote a higher formation energy DW to form instead. The 180° Y-DW showed the highest potential for conducting DWs in the structure, and the high formation energy compared to the 71° DW makes it unlikely to be formed. In addition, the transition levels of the defect in the DW should be investigated, in order to estimate the mobility of the introduced charge carriers. Charge carriers in deep states require much more energy to reach the conduction band than charge carriers in shallow states. As the band gap is much smaller in the DW than in bulk, charge carriers in the deep defect states would require less energy to become mobile. This effect is vital for the practical use of LaWN$_3$ as a FeRAM device, by using the conductivity of the DWs.

The Curie temperature of LaWN$_3$ was also estimated in this project through an empirical relationship with the displacement of tungsten in the bulk structure. However, due to the significant uncertainty in this value, a molecular dynamics study should be performed to investigate the transition from ground state to a high temperature non-polar phase, to get a better estimate of the T_c. This is important not only in order to get a deeper understanding of the properties of LaWN$_3$, but in addition understand the conductivity of the DWs, as a basis to investigate if thermal excitation of charge carriers from the valence band or nitrogen vacancies are possible in the DW.

Bibliography

[1] Sindre Mjøen Svendsen. 'Holes in the LaWN3'. In: *NTNU* (2023).

[2] A. M. Turing. 'On Computable Numbers, with an Application to the Entscheidungsproblem'. en. In: *Proceedings of the London Mathematical Society* s2-42.1 (1937), pp. 230–265. ISSN: 1460-244X. DOI: 10.1112/plms/s2-42.1.230. URL: https://onlinelibrary.wiley.com/doi/abs/10.1112/plms/s2-42.1.230 (visited on 02/06/2024).

[3] *The State of the Transistor in 3 Charts - IEEE Spectrum*. en. URL: https://spectrum.ieee.org/transistor-density (visited on 21/05/2024).

[4] *Here's how much Information Technology is causing Global Energy Consumption (infographic)*. en. Feb. 2020. URL: https://www.digitalinformationworld.com/2020/02/the-global-energy-consumption-of-information-technologies-infographic.html (visited on 20/05/2024).

[5] *Fact file: Computing is using more energy than ever*. en-US. Oct. 2023. URL: https://frontiergroup.org/resources/fact-file-computing-is-using-more-energy-than-ever/ (visited on 20/05/2024).

[6] *Norway Energy Information — Enerdata*. en. May 2024. URL: https://www.enerdata.net/estore/energy-market/norway/ (visited on 20/05/2024).

[7] H. Kohlstedt et al. 'Current status and challenges of ferroelectric memory devices'. In: *Microelectronic Engineering*. 14th biennial Conference on Insulating Films on Semiconductors 80 (June 2005), pp. 296–304. ISSN: 0167-9317. DOI: 10.1016/j.mee.2005.04.084. URL: https://www.sciencedirect.com/science/article/pii/S0167931705002236 (visited on 15/04/2024).

[8] T. Mikolajick et al. 'FeRAM technology for high density applications'. In: *Microelectronics Reliability* 41.7 (July 2001), pp. 947–950. ISSN: 0026-2714. DOI: 10.1016/S0026-2714(01)00049-X. URL: https://www.sciencedirect.com/science/article/pii/S002627140100049X (visited on 21/05/2024).

[9] Pankaj Sharma et al. 'Nonvolatile ferroelectric domain wall memory'. In: *Science Advances* 3.6 (June 2017). Publisher: American Association for the Advancement of Science, e1700512. DOI: 10.1126/sciadv.1700512. URL: https://www.science.org/doi/10.1126/sciadv.1700512 (visited on 20/05/2024).

[10] Denis Meier and Sverre Magnus Selbach. *Ferroelectric domain walls for nanotechnology — Nature Reviews Materials*. URL: https://www.nature.com/articles/s41578-021-00375-z (visited on 20/05/2024).

[11] 'The interface is still the device'. en. In: *Nature Materials* 11.2 (Feb. 2012). Publisher: Nature Publishing Group, pp. 91–91. ISSN: 1476-4660. DOI: 10.1038/nmat3244. URL: https://www.nature.com/articles/nmat3244 (visited on 20/05/2024).

[12] Carlos Moure and Octavio Peña. 'Recent advances in perovskites: Processing and properties'. In: *Progress in Solid State Chemistry* 43.4 (Dec. 2015), pp. 123–148. ISSN: 0079-6786. DOI: 10.1016/j.progsolidstchem.2015.09.001. URL: https://www.sciencedirect.com/science/article/pii/S0079678615000230 (visited on 08/04/2024).

[13]   *VESTA*. URL: https://jp-minerals.org/vesta/en/ (visited on 02/06/2024).

[14]   Robert M. Hazen. 'Perovskites'. In: *Scientific American* 258.6 (1988). Publisher: Scientific American, a division of Nature America, Inc., pp. 74–81. ISSN: 0036-8733. URL: https://www.jstor.org/stable/24989124 (visited on 17/12/2023).

[15]   Toyoto Sato et al. 'Extending the applicability of the Goldschmidt tolerance factor to arbitrary ionic compounds'. en. In: *Scientific Reports* 6.1 (Apr. 2016). Publisher: Nature Publishing Group, p. 23592. ISSN: 2045-2322. DOI: 10.1038/srep23592. URL: https://www.nature.com/articles/srep23592 (visited on 28/05/2024).

[16]   P. M. Woodward. 'Octahedral Tilting in Perovskites. I. Geometrical Considerations'. en. In: *Acta Crystallographica Section B* 53.1 (1997), pp. 32–43. ISSN: 1600-5740. DOI: 10.1107/S0108768196010713. URL: https://onlinelibrary.wiley.com/doi/abs/10.1107/S0108768196010713 (visited on 29/04/2024).

[17]   J. Paul Attfield, Philip Lightfoot and Russell E. Morris. 'Perovskites'. en. In: *Dalton Transactions* 44.23 (2015), pp. 10541–10542. ISSN: 1477-9226, 1477-9234. DOI: 10.1039/C5DT90083B. URL: http://xlink.rsc.org/?DOI=C5DT90083B (visited on 04/04/2024).

[18]   Shuang Liu et al. 'A Review on Additives for Halide Perovskite Solar Cells'. en. In: *Advanced Energy Materials* 10.13 (2020), p. 1902492. ISSN: 1614-6840. DOI: 10.1002/aenm.201902492. URL: https://onlinelibrary.wiley.com/doi/abs/10.1002/aenm.201902492 (visited on 14/04/2024).

[19]   *Distortion of Perovskites , Goldschmidt*. URL: http://www.ccp14.ac.uk/ccp/web-mirrors/pki/uni/pki/members/schinzer/stru_chem/perov/di_gold.html (visited on 31/05/2024).

[20]   Mahshid Ahmadi et al. 'Machine learning for high-throughput experimental exploration of metal halide perovskites'. en. In: *Joule* 5.11 (Nov. 2021), pp. 2797–2822. ISSN: 25424351. DOI: 10.1016/j.joule.2021.10.001. URL: https://linkinghub.elsevier.com/retrieve/pii/S2542435121004451 (visited on 10/04/2024).

[21]   Giulia Grancini and Mohammad Khaja Nazeeruddin. 'Dimensional tailoring of hybrid perovskites for photovoltaics'. en. In: *Nature Reviews Materials* 4.1 (Jan. 2019). Publisher: Nature Publishing Group, pp. 4–22. ISSN: 2058-8437. DOI: 10.1038/s41578-018-0065-0. URL: https://www.nature.com/articles/s41578-018-0065-0 (visited on 10/04/2024).

[22]   Yuheng Li and Kesong Yang. 'High-throughput computational design of halide perovskites and beyond for optoelectronics'. en. In: *WIREs Computational Molecular Science* 11.3 (2021), e1500. ISSN: 1759-0884. DOI: 10.1002/wcms.1500. URL: https://onlinelibrary.wiley.com/doi/abs/10.1002/wcms.1500 (visited on 10/04/2024).

[23]   Yicheng Zhao et al. 'Discovery of temperature-induced stability reversal in perovskites using high-throughput robotic learning'. en. In: *Nature Communications* 12.1 (Apr. 2021). Publisher: Nature Publishing Group, p. 2191. ISSN: 2041-1723. DOI: 10.1038/s41467-021-22472-x. URL: https://www.nature.com/articles/s41467-021-22472-x (visited on 10/04/2024).

[24] Simon D. Kloß, Martin L. Weidemann and J. Paul Attfield. 'Preparation of Bulk-Phase Nitride Perovskite LaReN3 and Topotactic Reduction to LaNiO2-Type LaReN2'. en. In: *Angewandte Chemie International Edition* 60.41 (2021), pp. 22260–22264. ISSN: 1521-3773. DOI: 10.1002/anie.202108759. URL: https://onlinelibrary.wiley.com/doi/abs/10.1002/anie.202108759 (visited on 11/04/2024).

[25] Mula Na et al. 'Improved quantum-mechanical model for evaluating the difficult synthesis of nitride and oxygen perovskites'. In: *Solid State Communications* 383 (May 2024), p. 115485. ISSN: 0038-1098. DOI: 10.1016/j.ssc.2024.115485. URL: https://www.sciencedirect.com/science/article/pii/S0038109824000620 (visited on 04/05/2024).

[26] Rachel Sherbondy et al. 'High-Throughput Selection and Experimental Realization of Two New Ce-Based Nitride Perovskites: CeMoN3 and CeWN3'. In: *Chemistry of Materials* 34.15 (Aug. 2022). Publisher: American Chemical Society, pp. 6883–6893. ISSN: 0897-4756. DOI: 10.1021/acs.chemmater.2c01282. URL: https://doi.org/10.1021/acs.chemmater.2c01282 (visited on 10/04/2024).

[27] Subhadeep Bandyopadhyay, Atanu Paul and I. Dasgupta. 'Origin of Rashba-Dresselhaus effect in the ferroelectric nitride perovskite ${\mathrm{LaWN}}_{3}$'. In: *Physical Review B* 101.1 (Jan. 2020). Publisher: American Physical Society, p. 014109. DOI: 10.1103/PhysRevB.101.014109. URL: https://link.aps.org/doi/10.1103/PhysRevB.101.014109 (visited on 10/04/2024).

[28] Xing Liu, Jia Fu and Guangming Chen. 'First-principles calculations of electronic structure and optical and elastic properties of the novel ABX 3 -type LaWN 3 perovskite structure'. en. In: *RSC Advances* 10.29 (2020). Publisher: Royal Society of Chemistry, pp. 17317–17326. DOI: 10.1039/C9RA10735E. URL: https://pubs.rsc.org/en/content/articlelanding/2020/ra/c9ra10735e (visited on 12/04/2024).

[29] Qi Ren et al. 'First-principles study of the lattice thermal conductivity of the nitride perovskite ${\mathrm{LaWN}}_{3}$'. In: *Physical Review B* 107.12 (Mar. 2023). Publisher: American Physical Society, p. 125206. DOI: 10.1103/PhysRevB.107.125206. URL: https://link.aps.org/doi/10.1103/PhysRevB.107.125206 (visited on 12/04/2024).

[30] Yue-Wen Fang et al. 'Lattice dynamics and ferroelectric properties of the nitride perovskite ${\mathrm{LaWN}}_{3}$'. In: *Physical Review B* 95.1 (Jan. 2017). Publisher: American Physical Society, p. 014111. DOI: 10.1103/PhysRevB.95.014111. URL: https://link.aps.org/doi/10.1103/PhysRevB.95.014111 (visited on 10/04/2024).

[31] C. N. W. Darlington and H. D. Megaw. 'Geometrical and structural relations in the rhombohedral perovskites'. en. In: *Acta Crystallographica Section A: Crystal Physics, Diffraction, Theoretical and General Crystallography* 31.2 (Mar. 1975). Publisher: International Union of Crystallography, pp. 161–173. ISSN: 0567-7394. DOI: 10.1107/S0567739475000332. URL: https://journals.iucr.org/a/issues/1975/02/00/a11672/ (visited on 31/05/2024).

[32] Rebecca W. Smaha et al. 'Structural and optoelectronic properties of thin film LaWN 3'. en. In: *Physical Review Materials* 7.8 (Aug. 2023), p. 084411. ISSN: 2475-9953. DOI: 10.1103/PhysRevMaterials.7.084411. URL: https://link.aps.org/doi/10.1103/PhysRevMaterials.7.084411 (visited on 12/04/2024).

[33] Huafeng Dong et al. 'Elastic properties of tetragonal BiFeO3 from first-principles calculations'. In: *Applied Physics Letters* 102.18 (May 2013), p. 182905. ISSN: 0003-6951. DOI: 10.1063/1.4804641. URL: https://doi.org/10.1063/1.4804641 (visited on 31/05/2024).

[34] Shining Geng and Zewen Xiao. 'Can Nitride Perovskites Provide the Same Superior Optoelectronic Properties as Lead Halide Perovskites?' In: *ACS Energy Letters* 8.4 (Apr. 2023). Publisher: American Chemical Society, pp. 2051–2057. DOI: 10.1021/acsenergylett.3c00658. URL: https://doi.org/10.1021/acsenergylett.3c00658 (visited on 12/04/2024).

[35] Santosh Singh and Madhvendra Nath Tripathi. 'Sr-doped LaMoN3 and LaWN3: New degenerate p-type nitrides'. In: *Journal of Applied Physics* 124.6 (Aug. 2018), p. 065109. ISSN: 0021-8979. DOI: 10.1063/1.5035135. URL: https://doi.org/10.1063/1.5035135 (visited on 14/04/2024).

[36] Guo-Xia Lai et al. 'Exploring Ferroelectric and Photovoltaic Attributes of Pna21-LaWN3: A First-Principles Approach'. In: *Physica B: Condensed Matter* (May 2024), p. 416084. ISSN: 0921-4526. DOI: 10.1016/j.physb.2024.416084. URL: https://www.sciencedirect.com/science/article/pii/S0921452624004253 (visited on 21/05/2024).

[37] Xuefeng Zhou et al. 'Polar Nitride Perovskite LaWN3- with Orthorhombic Structure'. en. In: *Advanced Science* 10.19 (2023), p. 2205479. ISSN: 2198-3844. DOI: 10.1002/advs.202205479. URL: https://onlinelibrary.wiley.com/doi/abs/10.1002/advs.202205479 (visited on 05/05/2024).

[38] Kevin R. Talley et al. 'Synthesis of LaWN3 nitride perovskite with polar symmetry'. In: *Science* 374.6574 (Dec. 2021). Publisher: American Association for the Advancement of Science, pp. 1488–1491. DOI: 10.1126/science.abm3466. URL: https://www.science.org/doi/full/10.1126/science.abm3466 (visited on 12/04/2024).

[39] Kota Hanzawa and Hidenori Hiramatsu. 'Heteroepitaxial Growth, Degenerate State, and Superconductivity of Perovskite-Type LaWN3 Thin Films'. In: *ACS Applied Electronic Materials* 5.5 (May 2023). Publisher: American Chemical Society, pp. 2793–2798. DOI: 10.1021/acsaelm.3c00249. URL: https://doi.org/10.1021/acsaelm.3c00249 (visited on 27/04/2024).

[40] V. K. Wadhawan. 'Towards a rigorous definition of ferroic phase transitions'. In: *Phase Transitions* 64.3 (Feb. 1998). Publisher: Taylor & Francis _eprint: https://doi.org/10.1080/01411599808220645, pp. 165–177. ISSN: 0141-1594. DOI: 10.1080/01411599808220645. URL: https://doi.org/10.1080/01411599808220645 (visited on 12/04/2024).

[41] Vincenzo Pasquale. 'Curie Temperature'. en. In: *Encyclopedia of Solid Earth Geophysics*. Ed. by Harsh K. Gupta. Series Title: Encyclopedia of Earth Sciences Series. Cham: Springer International Publishing, 2020, pp. 1–2. ISBN: 978-3-030-10475-7. DOI: 10.1007/978-3-030-10475-7_109-1. URL: http://link.springer.com/10.1007/978-3-030-10475-7_109-1 (visited on 05/04/2024).

[42] Stephanie Gnewuch and Efrain E. Rodriguez. 'The fourth ferroic order: Current status on ferrotoroidic materials'. In: *Journal of Solid State Chemistry* 271 (Mar. 2019), pp. 175–190. ISSN: 0022-4596. DOI: 10.1016/j.jssc.2018.12.035. URL: https://www.sciencedirect.com/science/article/pii/S0022459618305760 (visited on 05/04/2024).

[43] N. A. Spaldin and R. Ramesh. 'Advances in magnetoelectric multiferroics'. en. In: *Nature Materials* 18.3 (Mar. 2019). Publisher: Nature Publishing Group, pp. 203–212. ISSN: 1476-4660. DOI: 10.1038/s41563-018-0275-2. URL: https://www.nature.com/articles/s41563-018-0275-2 (visited on 05/04/2024).

[44] *Ferrotoroidic Order*. en. URL: https://ferroic.mat.ethz.ch/research/topics/ferroic-states-of-matter/ferrotoroidic-order.html (visited on 05/04/2024).

[45] J. F. Scott. 'Applications of Modern Ferroelectrics'. In: *Science* 315.5814 (Feb. 2007). Publisher: American Association for the Advancement of Science, pp. 954–959. DOI: 10.1126/science.1129564. URL: https://www.science.org/doi/full/10.1126/science.1129564 (visited on 05/04/2024).

[46] R. E. Newnham and S. Trolier-mckinstry. 'Size effects in ferroics'. In: *Integrated Ferroelectrics* 20.1-4 (Jan. 1998). Publisher: Taylor & Francis _eprint: https://doi.org/10.1080/10584589808238761, pp. 1–13. ISSN: 1058-4587. DOI: 10.1080/10584589808238761. URL: https://doi.org/10.1080/10584589808238761 (visited on 05/04/2024).

[47] Wenwu Cao and Clive A. Randall. 'Grain size and domain size relations in bulk ceramic ferroelectric materials'. In: *Journal of Physics and Chemistry of Solids*. Proceeding of the 3rd Williamsburg Workshop on Fundamental Experiments on Ferroelectrics 57.10 (Oct. 1996), pp. 1499–1505. ISSN: 0022-3697. DOI: 10.1016/0022-3697(96)00019-4. URL: https://www.sciencedirect.com/science/article/pii/0022369796000194 (visited on 28/05/2024).

[48] J. Seidel et al. 'Conduction at domain walls in oxide multiferroics'. en. In: *Nature Materials* 8.3 (Mar. 2009). Publisher: Nature Publishing Group, pp. 229–234. ISSN: 1476-4660. DOI: 10.1038/nmat2373. URL: https://www.nature.com/articles/nmat2373 (visited on 14/04/2024).

[49] E. J. Torok, A. L. Olson and H. N. Oredson. 'Transition between Bloch and Néel Walls'. In: *Journal of Applied Physics* 36.4 (Apr. 1965), pp. 1394–1399. ISSN: 0021-8979. DOI: 10.1063/1.1714317. URL: https://doi.org/10.1063/1.1714317 (visited on 04/06/2024).

[50] *Neumann's Principle*. en. Aug. 2014. URL: https://chem.libretexts.org/Bookshelves/Inorganic_Chemistry/Supplemental_Modules_and_Websites_(Inorganic_Chemistry)/Crystallography/Physical_Properties_of_Crystals/Neumann's_Principle (visited on 05/05/2024).

[51]   Mathias Schröder et al. 'Conducting Domain Walls in Lithium Niobate Single Crystals'. en. In: *Advanced Functional Materials* 22.18 (2012). _eprint: https://onlinelibrary.wiley.com/doi/pdf/10.1002/adfm.201201174, pp. 3936–3944. ISSN: 1616-3028. DOI: 10.1002/adfm.201201174. URL: https://onlinelibrary.wiley.com/doi/abs/10.1002/adfm.201201174 (visited on 14/04/2024).

[52]   G. F. Nataf et al. 'Domain-wall engineering and topological defects in ferroelectric and ferroelastic materials'. en. In: *Nature Reviews Physics* 2.11 (Nov. 2020). Publisher: Nature Publishing Group, pp. 634–648. ISSN: 2522-5820. DOI: 10.1038/s42254-020-0235-z. URL: https://www.nature.com/articles/s42254-020-0235-z (visited on 05/06/2024).

[53]   L. J. McGilly et al. 'Controlling domain wall motion in ferroelectric thin films'. en. In: *Nature Nanotechnology* 10.2 (Feb. 2015). Publisher: Nature Publishing Group, pp. 145–150. ISSN: 1748-3395. DOI: 10.1038/nnano.2014.320. URL: https://www.nature.com/articles/nnano.2014.320 (visited on 15/04/2024).

[54]   Anand Chandrasekaran et al. 'Defect ordering and defect–domain-wall interactions in PbTiO${}_{3}$: A first-principles study'. In: *Physical Review B* 88.21 (Dec. 2013). Publisher: American Physical Society, p. 214116. DOI: 10.1103/PhysRevB.88.214116. URL: https://link.aps.org/doi/10.1103/PhysRevB.88.214116 (visited on 15/04/2024).

[55]   Donghwa () Lee et al. 'Shape of ferroelectric domains in LiNbO3 and LiTaO3 from defect/domain-wall interactions'. In: *Applied Physics Letters* 98.9 (Mar. 2011), p. 092903. ISSN: 0003-6951. DOI: 10.1063/1.3560343. URL: https://doi.org/10.1063/1.3560343 (visited on 15/04/2024).

[56]   Donghwa () Lee, Venkatraman Gopalan and Simon R. Phillpot. 'Depinning of the ferroelectric domain wall in congruent LiNbO3'. In: *Applied Physics Letters* 109.8 (Aug. 2016), p. 082905. ISSN: 0003-6951. DOI: 10.1063/1.4961614. URL: https://doi.org/10.1063/1.4961614 (visited on 28/05/2024).

[57]   Michael Mansfield and Colm O'Sullivan. *Understanding physics*. 3rd edition. 2020.

[58]   David Sholl and Janice Steckel. *Density Functional Theory: A Practical Introduction*. 2009.

[59]   John P. Perdew et al. 'Restoring the Density-Gradient Expansion for Exchange in Solids and Surfaces'. In: *Physical Review Letters* 100.13 (Apr. 2008). Publisher: American Physical Society, p. 136406. DOI: 10.1103/PhysRevLett.100.136406. URL: https://link.aps.org/doi/10.1103/PhysRevLett.100.136406 (visited on 27/11/2023).

[60]   Chun-Gang Duan et al. 'Electronic, magnetic and transport properties of rare-earth monopnictides'. en. In: *Journal of Physics: Condensed Matter* 19.31 (July 2007), p. 315220. ISSN: 0953-8984. DOI: 10.1088/0953-8984/19/31/315220. URL: https://dx.doi.org/10.1088/0953-8984/19/31/315220 (visited on 16/05/2024).

[61]   G. Kresse and D. Joubert. 'From ultrasoft pseudopotentials to the projector augmented-wave method'. en. In: *Physical Review B* 59.3 (Jan. 1999), pp. 1758–1775. ISSN: 0163-1829, 1095-3795. DOI: 10.1103/PhysRevB.59.1758. URL: https://link.aps.org/doi/10.1103/PhysRevB.59.1758 (visited on 27/11/2023).

[62] *VASP - Vienna Ab initio Simulation Package*. URL: https://www.vasp.at/ (visited on 27/11/2023).

[63] *2.4.2 Kröger-Vink Notation*. URL: https://www.tf.uni-kiel.de/matwis/amat/def_en/kap_2/backbone/r2_4_2.html (visited on 06/06/2024).

[64] William Callister Jr and David Rethwisch. *Materials Science and Engineering*. 9th edition. 2015.

[65] Klichchupong Dabsamut, Adisak Boonchun and Walter R. L. Lambrecht. 'First-principles study of n- and p-type doping opportunities in LiGaO2'. en. In: *Journal of Physics D: Applied Physics* 53.27 (May 2020). Publisher: IOP Publishing, p. 274002. ISSN: 0022-3727. DOI: 10.1088/1361-6463/ab8514. URL: https://dx.doi.org/10.1088/1361-6463/ab8514 (visited on 16/05/2024).

[66] Naseem Ud Din et al. *Defects and Oxygen Impurities in Ferroelectric Wurtzite Al$_{1-x}$Sc$_x$N Alloys*. arXiv:2308.14310 [cond-mat]. Aug. 2023. DOI: 10.48550/arXiv.2308.14310. URL: http://arxiv.org/abs/2308.14310 (visited on 21/04/2024).

[67] Stephan Lany and Alex Zunger. 'Assessment of correction methods for the band-gap problem and for finite-size effects in supercell defect calculations: Case studies for ZnO and GaAs'. In: *Physical Review B* 78.23 (Dec. 2008). Publisher: American Physical Society, p. 235104. DOI: 10.1103/PhysRevB.78.235104. URL: https://link.aps.org/doi/10.1103/PhysRevB.78.235104 (visited on 15/04/2024).

[68] Anuj Goyal et al. 'A computational framework for automation of point defect calculations'. In: *Computational Materials Science* 130 (Apr. 2017), pp. 1–9. ISSN: 0927-0256. DOI: 10.1016/j.commatsci.2016.12.040. URL: https://www.sciencedirect.com/science/article/pii/S0927025617300010 (visited on 15/04/2024).

[69] Graeme Henkelman and Hannes Jónsson. 'Improved tangent estimate in the nudged elastic band method for finding minimum energy paths and saddle points'. en. In: *The Journal of Chemical Physics* 113.22 (Dec. 2000), pp. 9978–9985. ISSN: 0021-9606, 1089-7690. DOI: 10.1063/1.1323224. URL: https://pubs.aip.org/jcp/article/113/22/9978/184858/Improved-tangent-estimate-in-the-nudged-elastic (visited on 08/05/2024).

[70] Graeme Henkelman, Blas P. Uberuaga and Hannes Jónsson. 'A climbing image nudged elastic band method for finding saddle points and minimum energy paths'. en. In: *The Journal of Chemical Physics* 113.22 (Dec. 2000), pp. 9901–9904. ISSN: 0021-9606, 1089-7690. DOI: 10.1063/1.1329672. URL: https://pubs.aip.org/jcp/article/113/22/9901/185050/A-climbing-image-nudged-elastic-band-method-for (visited on 08/05/2024).

[71] H. D. Megaw and C. N. W. Darlington. 'Geometrical and structural relations in the rhombohedral perovskites'. en. In: *Acta Crystallographica Section A: Crystal Physics, Diffraction, Theoretical and General Crystallography* 31.2 (Mar. 1975). Publisher: International Union of Crystallography, pp. 161–173. ISSN: 0567-7394. DOI: 10.1107/S0567739475000332. URL: //scripts.iucr.org/cgi-bin/paper?a11672 (visited on 11/04/2024).

[72] John Buckeridge. *jbuckeridge/cplap*. original-date: 2013-06-05T15:25:10Z. Dec. 2023. URL: https://github.com/jbuckeridge/cplap (visited on 29/04/2024).

[73] Samuel T. Murphy and Nicholas D. M. Hine. 'Anisotropic charge screening and supercell size convergence of defect formation energies'. In: *Physical Review B* 87.9 (Mar. 2013). Publisher: American Physical Society, p. 094111. DOI: 10.1103/PhysRevB.87.094111. URL: https://link.aps.org/doi/10.1103/PhysRevB.87.094111 (visited on 19/05/2024).

[74] Shi Liu, Ilya Grinberg and Andrew M. Rappe. 'Intrinsic ferroelectric switching from first principles'. en. In: *Nature* 534.7607 (June 2016). Publisher: Nature Publishing Group, pp. 360–363. ISSN: 1476-4687. DOI: 10.1038/nature18286. URL: https://www.nature.com/articles/nature18286 (visited on 10/05/2024).

[75] Axel Lubk, S. Gemming and N. A. Spaldin. 'First-principles study of ferroelectric domain walls in multiferroic bismuth ferrite'. In: *Physical Review B* 80.10 (Sept. 2009). Publisher: American Physical Society, p. 104110. DOI: 10.1103/PhysRevB.80.104110. URL: https://link.aps.org/doi/10.1103/PhysRevB.80.104110 (visited on 14/05/2024).

[76] Xueyou Zhang et al. 'First-principles calculations of domain wall energies of prototypical ferroelectric perovskites'. In: *Acta Materialia* 242 (Jan. 2023), p. 118351. ISSN: 1359-6454. DOI: 10.1016/j.actamat.2022.118351. URL: https://www.sciencedirect.com/science/article/pii/S1359645422007303 (visited on 10/05/2024).

[77] Shi Liu et al. 'Ferroelectric Domain Wall Induced Band Gap Reduction and Charge Separation in Organometal Halide Perovskites'. In: *The Journal of Physical Chemistry Letters* 6.4 (Feb. 2015). Publisher: American Chemical Society, pp. 693–699. DOI: 10.1021/jz502666j. URL: https://doi.org/10.1021/jz502666j (visited on 11/05/2024).

[78] Jan Seidel et al. 'Domain wall functionality in BiFeO3'. In: *Phase Transitions* 86.1 (Jan. 2013), pp. 53–66. ISSN: 0141-1594. DOI: 10.1080/01411594.2012.695371. URL: https://doi.org/10.1080/01411594.2012.695371 (visited on 13/05/2024).

[79] Ekhardt K.H Salje. *Phase transitions in ferroelastic and co-elastic crystals*. Student edition. 1993.

[80] S. C. Abrahams, S. K. Kurtz and P. B. Jamieson. 'Atomic Displacement Relationship to Curie Temperature and Spontaneous Polarization in Displacive Ferroelectrics'. In: *Physical Review* 172.2 (Aug. 1968). Publisher: American Physical Society, pp. 551–553. DOI: 10.1103/PhysRev.172.551. URL: https://link.aps.org/doi/10.1103/PhysRev.172.551 (visited on 23/05/2024).

[81] Eggestad Eggestad et al. 'Mobile Intrinsic Point Defects for Conductive Neutral Domain Walls in LiNbO3'. In: ().

[82] Petr S. Bednyakov et al. 'Physics and applications of charged domain walls'. en. In: *npj Computational Materials* 4.1 (Nov. 2018). Publisher: Nature Publishing Group, pp. 1–11. ISSN: 2057-3960. DOI: 10.1038/s41524-018-0121-8. URL: https://www.nature.com/articles/s41524-018-0121-8 (visited on 19/05/2024).

[83]   S. Farokhipoor and B. Noheda. 'Conduction through 71° Domain Walls in ${\mathrm{BiFeO}}_{3}$ Thin Films'. In: *Physical Review Letters* 107.12 (Sept. 2011). Publisher: American Physical Society, p. 127601. DOI: 10.1103/PhysRevLett.107.127601. URL: https://link.aps.org/doi/10.1103/PhysRevLett.107.127601 (visited on 14/05/2024).

[84]   Tadej Rojac et al. 'Domain-wall conduction in ferroelectric BiFeO3 controlled by accumulation of charged defects'. en. In: *Nature Materials* 16.3 (Mar. 2017). Publisher: Nature Publishing Group, pp. 322–327. ISSN: 1476-4660. DOI: 10.1038/nmat4799. URL: https://www.nature.com/articles/nmat4799 (visited on 25/05/2024).

[85]   Satoru Matsuishi, Daiki Iwasaki and Hideo Hosono. 'Synthesis of perovskite-type LaWN3 by high-pressure solid-state metathesis reaction'. In: *Journal of Solid State Chemistry* 315 (Nov. 2022), p. 123508. ISSN: 0022-4596. DOI: 10.1016/j.jssc.2022.123508. URL: https://www.sciencedirect.com/science/article/pii/S0022459622006338 (visited on 19/05/2024).

[86]   Tam T. Mayeshiba and Dane D. Morgan. 'Factors controlling oxygen migration barriers in perovskites'. In: *Solid State Ionics* 296 (Nov. 2016), pp. 71–77. ISSN: 0167-2738. DOI: 10.1016/j.ssi.2016.09.007. URL: https://www.sciencedirect.com/science/article/pii/S0167273816304088 (visited on 19/05/2024).

[87]   *Shannon Radii*. URL: http://abulafia.mt.ic.ac.uk/shannon/ptable.php (visited on 31/05/2024).

[88]   A. Zobelli et al. 'Vacancy migration in hexagonal boron nitride'. In: *Physical Review B* 75.9 (Mar. 2007). Publisher: American Physical Society, p. 094104. DOI: 10.1103/PhysRevB.75.094104. URL: https://link.aps.org/doi/10.1103/PhysRevB.75.094104 (visited on 19/05/2024).

[89]   Sukit Limpijumnong and Chris G. Van de Walle. 'Diffusivity of native defects in GaN'. In: *Physical Review B* 69.3 (Jan. 2004). Publisher: American Physical Society, p. 035207. DOI: 10.1103/PhysRevB.69.035207. URL: https://link.aps.org/doi/10.1103/PhysRevB.69.035207 (visited on 19/05/2024).

[90]   Hongxia Bu et al. 'The role of sp2 and sp3 hybridized bonds on the structural, mechanical, and electronic properties in a hard BN framework'. en. In: *RSC Advances* 9.5 (Jan. 2019). Publisher: The Royal Society of Chemistry, pp. 2657–2665. ISSN: 2046-2069. DOI: 10.1039/C8RA09636H. URL: https://pubs.rsc.org/en/content/articlelanding/2019/ra/c8ra09636h (visited on 25/05/2024).

[91]   Roger A. De Souza, M. Saiful Islam and Ellen Ivers-Tiffée. 'Formation and migration of cation defects in the perovskite oxide LaMnO 3'. en. In: *Journal of Materials Chemistry* 9.7 (1999). Publisher: Royal Society of Chemistry, pp. 1621–1627. DOI: 10.1039/A901512D. URL: https://pubs.rsc.org/en/content/articlelanding/1999/jm/a901512d (visited on 19/05/2024).

[92]   Grégory Geneste, Charles Paillard and Brahim Dkhil. *Phys. Rev. B 99, 024104 (2019) - Polarons, vacancies, vacancy associations, and defect states in multiferroic ${\mathrm{BiFeO}}_{3}$*. URL: https://journals.aps.org/prb/abstract/10.1103/PhysRevB.99.024104 (visited on 25/05/2024).

Appendix

A   Previous results

Convergence test for k-points and cutoff energy done in previous work [1].
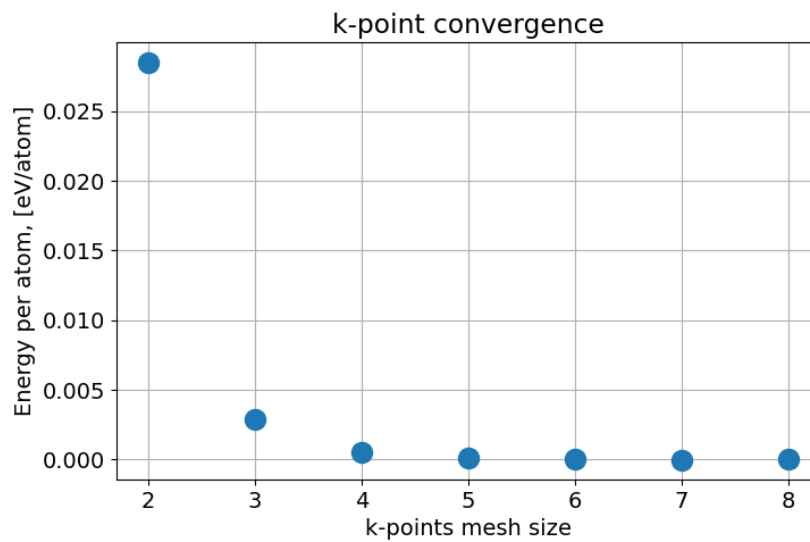
Figure A.1: k-point convergence test
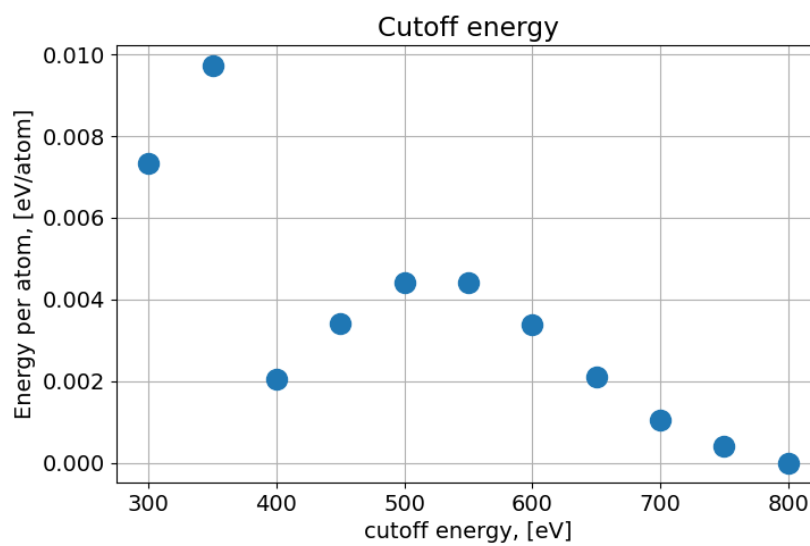
Figure A.2: Cutoff energy test

The dielectric tensor calculated in previous work[1] for bulk $R3c$ LaWN$_3$ in the conventional cell:

$$\varepsilon_{ij}^0 = \begin{pmatrix} 114.36 & 0 & 0 \\ 0 & 114.36 & 0 \\ 0 & 0 & 42.06 \end{pmatrix} \tag{A.1}$$

The result from the structural optimization of the pure elements is

Table A.1: Computed energies of pure elements and formation energy of competing phases.

Compound	Space group	Energy/Formation energy [eV]
La	$P6_3/mmc$	-5.356
W	$Im\bar{3}m$	-13.801
N		-8.532
O		-5.140
LaN	$Fm\bar{3}m$	-2.817
WN$_2$	$P6_3/mmc$	-1.532
LaWN$_3$	$R3c$	-5.890

B   Defect calculations

Figure B.1: Displacement of atoms in the V_{La} supercell from their original position, denoted ΔS, as a function of distance from the defect site

Figure B.2: Displacement of atoms in the V_N supercell from their original position, denoted ΔS, as a function of distance from the defect site

Figure B.3: Displacement of atoms in the La$_W$ supercell from their original position, denoted ΔS, as a function of distance from the defect site
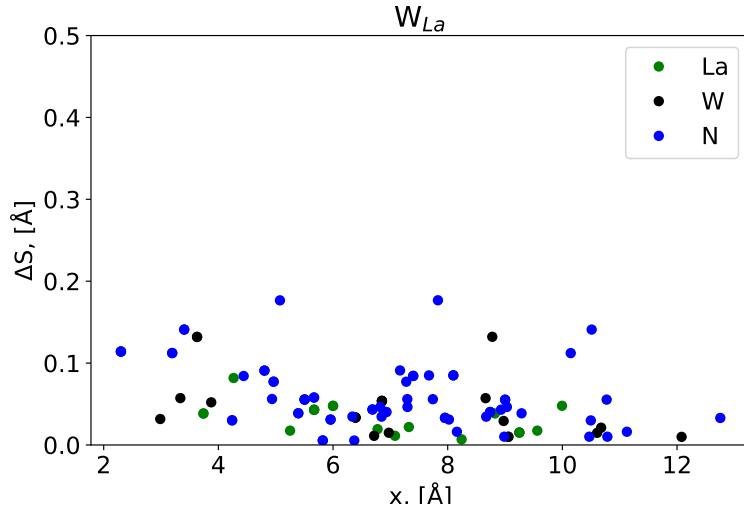
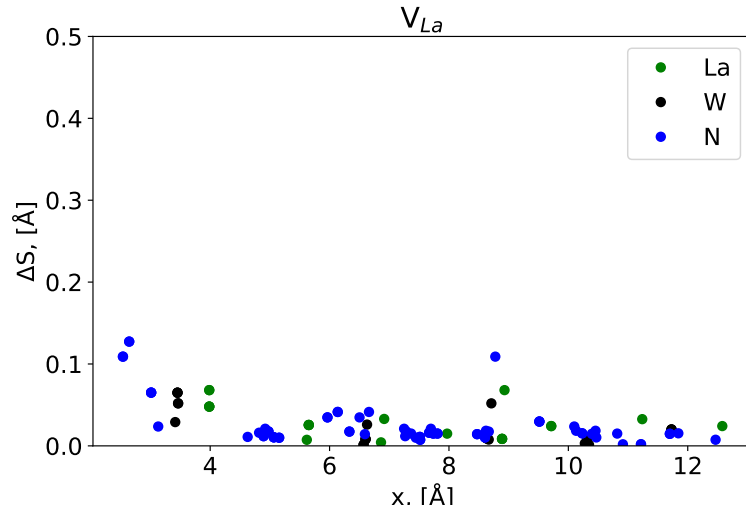Figure B.4: Displacement of atoms in the W$_{La}$ supercell from their original position, denoted ΔS, as a function of distance from the defect site
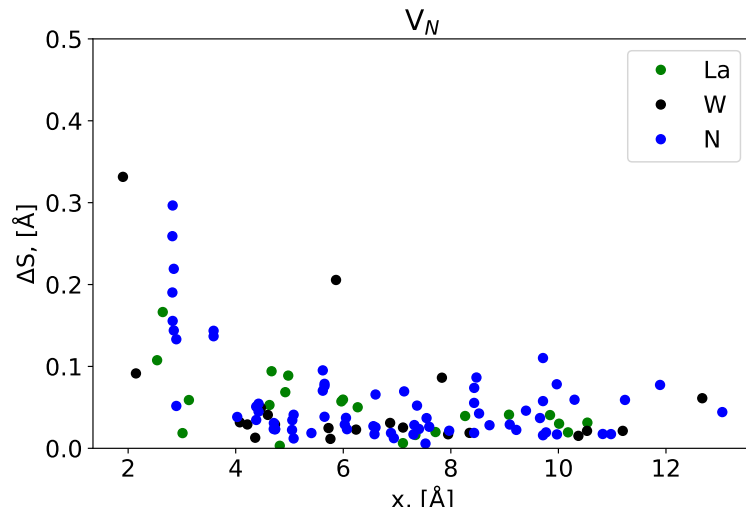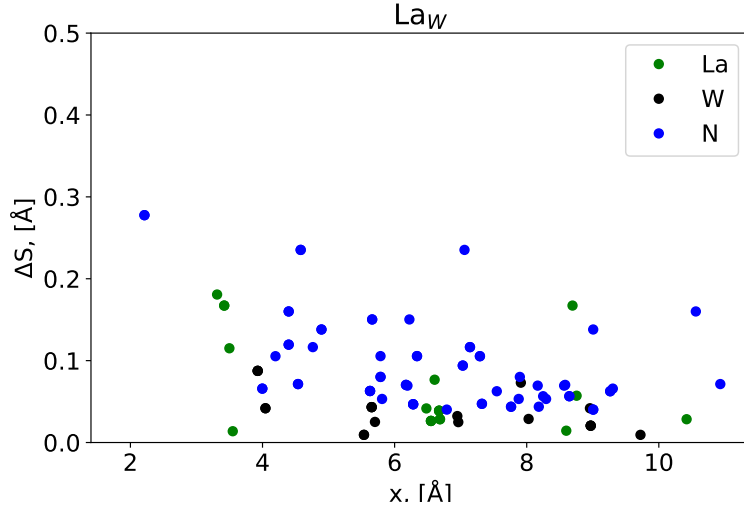
The baseline parameters found for bulk $R3c$ is

Table B.1: Cell values for the structural optimized supercell.

Cell energy	-1215.5098
E_{vbm}	8.7111

The calculated energies and corrections are

Table B.2: Cell values and corrections for defect supercell.

Defect	Cell charge	Cell energy	$\mathbf{E}_{cor}^{pot}$	$q^2\mathbf{E}_{cor}^{IC}$	$\mathbf{E}_{cor}^{BF}$
V_{La}	0	-1201.157	-0.313262	0	-0.0906
	-1	-1192.8217	-0.297751	0.010701	-0.0627
	-2	-1184.4366	-0.282011	0.042804	-0.0321
	-3	-1176.0368	-0.266179	0.096309	0
V_N	0	-1206.0289	-0.028003	0	0
	1	-1215.449	-0.039414	0.010701	0
	2	-1224.7472	-0.050625	0.042804	0
	3	-1234.1531	-0.061228	0.096309	0
La_W	0	-1201.9882	0.093956	0	-0.1060
	-1	-1193.241	0.110709	0.010701	-0.0919
	-2	-1184.5131	0.126941	0.042804	-0.0793
	-3	-1175.3013	0.141281	0.096309	0
W_{La}	0	-1218.5222	-0.111231	0	0.0000
	1	-1227.764	-0.11796	0.010701	0.0000
	2	-1237.0222	-0.131592	0.042804	0.0000
	3	-1245.9848	-0.144762	0.096309	0
O_N	0	-1215.07492	-0.173339	0	-0.0251
	1	-1224.6927	-0.176477	0.010701	0

C   Scripts

CPLAP

```
# To run this calculation (for the system BaSnO3) do:
#
# cp SAMPLE_INPUT input.dat
# ./CPLAP
#
# One competing phase has been left out - to add it in:
#
# cp results.dat restart.dat
# ./CPLAP
#
# and select option (b) (cp SAMPLE_EXTRA_PHASES extra_phases.dat first)
#
#
# First give number of species in the compound of interest
#
3
#
# Next give the formula and enthalpy of formation (E1) of the compound
# in the format:
#
# n_A A n_B B n_C C ... E1
#
# where n_A is the number of species A in the formula unit etc (E1
# is a negative number)
# (e.g. if the material is calcite then 1 Ca 1 C 3 O and then the
# energy must be entered. Please keep the energy units consistent
# when entering all data)
#
1 La 1 W 3 N -5.890
#
# Now enter which element is to be set as the dependent variable (i.e.
# given in terms of the other chemical potentials). If none is to be set,
# then write "none" (case sensitive) - note if no dependent variable is
# set then only the intersection points with the compound of interest
# are relevant
#
none
#
# Next give the number of competing phases to be considered:
#
2
#
# For each competing phase first give the number of species, then
# the formula of the compound
#
2
1 La 1 N -2.817
2
1 W 2 N -1.532
```

Figure C.1: CPLAP input. Lines with "#" are commented out.

```
****************************************************************************
**

Results for system:  1 La  1 W   3 N

Number of species:  3

Number of competing phases:  2

DATE:  20/ 2/2024   14:59:46

****************************************************************************
**

Energy: -0.5890000000000E+01 eV

Dependent variable:   none

****************************************************************************
**

Limiting inequalities:

    1.000 mu_La     1.000 mu_W      3.000 mu_N   =     -5.8900
    1.000 mu_La     0.000 mu_W      1.000 mu_N   <     -2.8170
    0.000 mu_La     1.000 mu_W      2.000 mu_N   <     -1.5320
    1.000 mu_La                                  <      0.0000
                    1.000 mu_W                   <      0.0000
                                    3.000 mu_N   <      0.0000
    1.000 mu_La                                  >     -5.8900
                    1.000 mu_W                   >     -5.8900
                                    3.000 mu_N   >     -5.8900

****************************************************************************
**

Intersection points in chemical potential space:

    mu_La      mu_W    |    mu_N  =
----------------------|-----------
   -1.2805     0.0000 |   -1.5365
   -2.8170    -3.0730 |    0.0000
   -3.5920     0.0000 |   -0.7660
   -4.3580    -1.5320 |    0.0000
   -2.0510     0.0000 |   -1.2797
   -2.8170    -1.5320 |   -0.5137

****************************************************************************
**

Competing phase   1 :   LaN   ( energy =   -2.8170 )
----------------------

Equation:

     1.0000 mu_La  +     1.0000 mu_N  =    -2.8170

Relevant intersection points:

    mu_La      mu_W    |    mu_N  >=
----------------------|-----------
   -1.2805     0.0000 |   -1.5365
   -2.8170    -3.0730 |    0.0000
   -2.0510     0.0000 |   -1.2797
```

```
   -2.8170    -1.5320 |   -0.5137
```
_____

––

```
Competing phase   2 :   WN2   ( energy =   -1.5320 )
-----------------------

Equation:

     1.0000 mu_W  +     2.0000 mu_N  =    -1.5320

Relevant intersection points:

   mu_La      mu_W   |   mu_N  >=
----------------------|-----------
   -3.5920     0.0000 |   -0.7660
   -4.3580    -1.5320 |    0.0000
   -2.0510     0.0000 |   -1.2797
   -2.8170    -1.5320 |   -0.5137
```
_____

––

```
Limits from system    :   LaWN3   ( energy =   -5.8900 )
-----------------------

Equation:

     1.0000 mu_La  +     1.0000 mu_W  +     3.0000 mu_N  =    -5.8900

Relevant intersection points:

   mu_La      mu_W   |   mu_N  >=
----------------------|-----------
   -1.2805     0.0000 |   -1.5365
   -2.8170    -3.0730 |    0.0000
   -3.5920     0.0000 |   -0.7660
   -4.3580    -1.5320 |    0.0000

****************************************************************************
**
```

Figure C.2: Result from CPLAP analysis.